Taiwan mountain building: insights from 2-D thermomechanical modelling of a rheologically stratified lithosphere

Philippe Yamato, Frédéric Mouthereau, Evgenii Burov

Geophys. J. Int. (2009) **176,** 307–326 doi: 10.1111/j.1365-246X.2008.03977.x

Taiwan mountain building: insights from 2-D thermomechanical modelling of a rheologically stratified lithosphere

P. Yamato,[1] F. Mouthereau[2] and E. Burov[2]

[1] *Geosciences Rennes,* UMR 6118 CNRS*, Université de Rennes* 1*,* 35042 *Rennes Cedex, France*
[2] *Laboratoire de tectonique, Université Pierre et Marie Curie—Paris* 6*,* UMR 7072 CNRS, 4 *place Jussieu,* F-75005 *Paris, France.*
E-mail: frederic.mouthereau@lgs.jussieu.fr

Accepted 2008 September 12. Received 2008 September 11; in original form 2008 January 5

SUMMARY

The Taiwan orogen has long been regarded as a case example for studying mountain building in association with subduction processes. In this paper, we present a fully coupled thermomechanical modelling of the Taiwan collision based on a realistic viscous-elastic–plastic rheology. It satisfactorily reproduces available thermochronometric data, long-/short-term deformation patterns, heat flux and erosion/sedimentation distribution across the Taiwan orogeny. We found that a deep seated flux of Asian crustal material into the orogenic wedge should be invoked to counter-balance observed exhumation and erosion in the Central Range. However, in contrast with recent thermokinematic models of exhumation and deformation suggesting that underplating plays a significant role, we show that most constraints on exhumation and deformation can be more straightforwardly interpreted by the frontal accretion of the rheologically layered Asian crust. We finally infer that such a model is in better agreement with the basic expectation that the hot/young and buoyant Chinese continental margin should hardly be subducted beneath the cold/old and dense oceanic plate of the Philippines Sea.

Key words: Mechanics, theory, and modelling; Rheology: crust and lithosphere.

1 INTRODUCTION

Since the studies by Davis *et al.* (1983) and Dahlen *et al.* (1984) that popularized the critically tapered wedges approach of mountain building, Taiwan has become the key natural example of mountain belts for the development of critical wedge model. Assuming steady-state evolution, thermokinematic models presented in foremost papers by Barr & Dahlen (1989) and Dahlen & Barr (1989) have allowed for comparison between predicted particle paths entering orogenic wedges and observed *P–T* conditions, temperature distribution and heat flux with several applications to Taiwan. More recently, the increasing number of thermochronometric constraints has renewed our interest in investigating the mechanisms of exhumation in the Taiwan mountain belt (Willett & Brandon 2002; Willett *et al.* 2003; Fuller *et al.* 2006; Simoes & Avouac 2006; Simoes *et al.* 2007). One major conclusion brought by these recent models is that underplating can represent 50 to 100 per cent of the materials accreted to the Taiwan orogenic wedge, which is significantly larger than the initially proposed 10–25 per cent of underplating (Barr & Dahlen 1989).

Much of the models cited above are thermokinematic models in which the temperature is solved to allow for comparison with available thermochronometric or metamorphic data. They are not designed for the full description of mechanical processes during long-term orogenic processes. Actually, few models intended to produce a mechanically comprehensive representation of the Taiwan Mountain building so far. Chemenda *et al.* (2001) proposed an original analogue modelling approach in 2-D and 3-D in which oceanic and continental lithospheres have distinct plastic behaviour and overlie a low-viscosity asthenosphere. These models satisfactorily explain several particular tectonic features of Taiwan. First, they are successful in reproducing the so-called 'Taiwan paradox', that is, the apparent contradiction between the relative normal motion along the plate boundary fault and the observation that 30 per cent of the plate convergence is accommodated across this fault. Second, it also successfully reproduced the subduction reversal, its initiation being indirectly constrained by the age of the onset of a strong subsidence on the upper Philippine Sea Plate (PSP). Third, a major conclusion brought by the works of Chemenda *et al.* (2001) but less discussed by the authors is the limited subduction of the continental crust beneath the overriding plate. Indeed, as soon as the continental crust is subducted, collision processes initiate and the rapid exhumation or extrusion of the continental basement takes place. Thus, Chemenda's model disagrees with a long-standing continental subduction beneath Taiwan and rather predicts that Taiwan is the result of a transient collisional stage.

Unfortunately, this type of models was not designed to allow for comparison with the thermochronometric data such as the metamorphic grades observed throughout the belt or the fission-track age constraints. Furthermore, it is not accurate enough to provide quantitative interpretations of long-term deformation or short-term GPS-derived deformation patterns. Finally, because the lithosphere

rheology is limited to plasticity, exhumation processes assisted by viscous flow of rocks were not taken into account, which is, however, known to be a likely phenomenon in orogenies controlled by high erosion rates (Beaumont *et al.* 2001).

Fuller *et al.* (2006) presented a 2-D thermomechanical numerical modelling of the evolution of the Taiwan orogen constrained by thermochronometric data. The rheology of the crust is more realistic than numerical models already mentioned. A power-law viscosity is preferred at high temperature and a Coulomb criterion is used to simulate plastic failure in the crust. This model is also more sophisticated since it is able to provide thermal constraints and thus allows for comparison between predicted *P–T* paths and observations. However, owing to boundary conditions, there are some limitations for applying this category of models. Indeed, the plate boundary geometry between the subducting and the overriding plates, for example, the slab dip and the geometry of the backstop are fixed. Moreover, the deformation within the crustal wedge is quasi-static so large deformations are not permitted and changes in material fluxes are only permitted at the base of the growing orogenic wedge and at the surface where erosional processes are considered. More critical to our study is that underplating is simulated by adding numerically an upward velocity of particles (Fuller *et al.* 2006; Simoes *et al.* 2007). Thus, the flux of accretion by underplating and the width of the underplating window are imposed directly by initial boundary conditions rather than being outputs of the model.

Based on this brief review it appears that any further studies dealing with the modelling of the Taiwan mountain building require 2-D (ideally 3-D) fully-coupled thermomechanical modelling. Moreover, thermomechanical modelling of such subduction/collision processes becomes more and more common and sophisticated (e.g. Burov *et al.* 2001; Burg & Gerya 2005; Sobolev & Babeyko 2005; Currie *et al.* 2007; Faccenda *et al.* 2008; Gerya *et al*. 2008; Yamato *et al*. 2007, 2008; Warren *et al.* 2008). However, in relation to Taiwan, only a first attempt at using such kind of thermomechanical model with viscous-plastic and viscous-elastic–plastic rheology has been recently presented (Kaus *et al.* 2008).

In this paper, our objective is to provide a 2-D thermomechanical numerical model of Taiwan mountain building at the lithospheric-scale that accounts for a wide range of natural observations. All the dynamic parameters are fully coupled so that velocities, strength and the plate geometry change with model evolution. In this paper, we attempt to account for structural, metamorphic and thermochronometric data as well as fitting the short-/long-term shortening distribution, erosion–sedimentation distribution, heat flow data, which has never been attempted so far.

2 TECTONIC AND GEOLOGICAL SETTING

2.1 Overview

The Taiwan collision results from the convergence between the downgoing Chinese continental margin belonging to the Eurasian plate and the overriding oceanic PSP (Fig. 1). The collision likely started in the late Miocene–early Pliocene (Suppe 1981; Ho 1986; Lin *et al.* 2003; Tensi *et al.* 2006) about 20Myr after the initiation of the oceanic spreading in the South China Sea (Lee & Lawver 1995; Clift *et al.* 2002; Lin *et al.* 2003). The present-day convergence rate of the Luzon Arc relative to the Chinese continental margin is estimated to be 80 mmyr^{-1} in N58°W direction (e.g. Yu *et al.* 1997).

The Taiwan Island is classically divided into several tectonic units (Ho 1986). The Coastal Range (CoR) to the East, which represents a part of the northern Luzon Arc, accreted to the collided margin (Fig. 2). The CoR consists of a Miocene magmatic basement arc associated with intra-arc turbidites. This sequence is overlain by thick Plio-Pleistocene synorogenic deposits (3–4 km) that derived from the erosion of the Taiwan mountain belt (Huang *et al.* 1995). The Longitudinal Valley Fault (LVF) is the plate boundary fault between the CoR and the Central Range. The latter comprises the exhumed Palaeozoic–Mesozoic metamorphic basement (Tananao Schist, TS) that is overlain by the Palaeogene and Neogene slates of the Backbone Range (BR) and the Hsuehshan Range (HR). The western non-metamorphic fold–thrust belt, namely the Western Foothills (WF) is made of foreland and marginal deposits accreted to the growing orogenic wedge during the Pliocene. Further west, the Coastal Plain (CP) lies at the transition between the frontal thrust units and the western foredeep (Fig. 2). Much of the currently active faults or Quaternary faults are located between the CP and the WF (Bonilla 1977). The Chichi earthquake ($M_l = 7.6$) that occurred on 1999 September 21, related to the reactivation of a large reverse fault rupture, the Chelungpu–Sani Fault (CST in Fig. 2), constitutes a remarkable example for the seismic release of a significant part of the current plate convergence.

2.2 Metamorphic conditions and thermochronometric constraints

The TS contains black schists, marbles and gneiss bodies, which present the highest *P–T* metamorphic conditions recorded in Taiwan. After the Nanao orogeny in the Late Mesozoic, during which the TS recorded amphibolites metamorphism, the TS units were secondarily overprinted, during the Mio-Pliocene Penglai orogeny, by an upper to lower grade greenschist facies metamorphism (Fig. 2). The temperature–time history predicted for the Chipan gneiss in the north of the TS and *P–T–t* paths calculated by wedge modelling (Barr & Dahlen 1989; Simoes *et al.* 2007) show consistent peak metamorphism (up to $T = 500$°C and $P =$ 6–8 kb) and cooling history. Although these models suggest heating and burial prior to exhumation, only few Ar^{40}/Ar^{39} ages on biotite (Lo & Onstott 1995) allow the identification of a prograde path in the Chipan gneiss *P–T* history. Also, little evidence is found of high-pressure (HP) metamorphic facies. They are restricted to kilometric-scale exotic blocks of glaucophane schists (e.g. Juisui blueschist) in the Yuli Belt (Fig. 2). They are interpreted as oceanic rocks metamorphosed under HP–LT conditions ($T = 450$–500°C, $P > 8$ kb) possibly during the Late Miocene (Ernst 1981). In light of more recent thermodynamic databases, peak metamorphic conditions have been re-evaluated to $T = 550$°C and $P = 10$–12 kb (Beyssac *et al.* 2008). These authors further suggested that these HP rocks have been exhumed in two steps the final exhumation having occurred between 10 and 4.5 Ma.

Fig. 3 shows a synthesis of the thermochronometric constraints in Taiwan. Samples with ages lower than 5Myr are believed to be reset ages as they cooled through the closure isotherm of the studied thermochronometer. Predicted unreset ages are assumed to be close to depositional ages. We have arbitrarily fixed unreset ages to 30Myr, which is the averaged stratigraphic age for Palaeogene sediments where samples have been collected.

Cooling apatite fission track (AFT) ages in the TS are generally younger than 1Ma (Fig. 3a). Determination of zircon fission track (ZFT) ages also show reset zircons but with slightly older

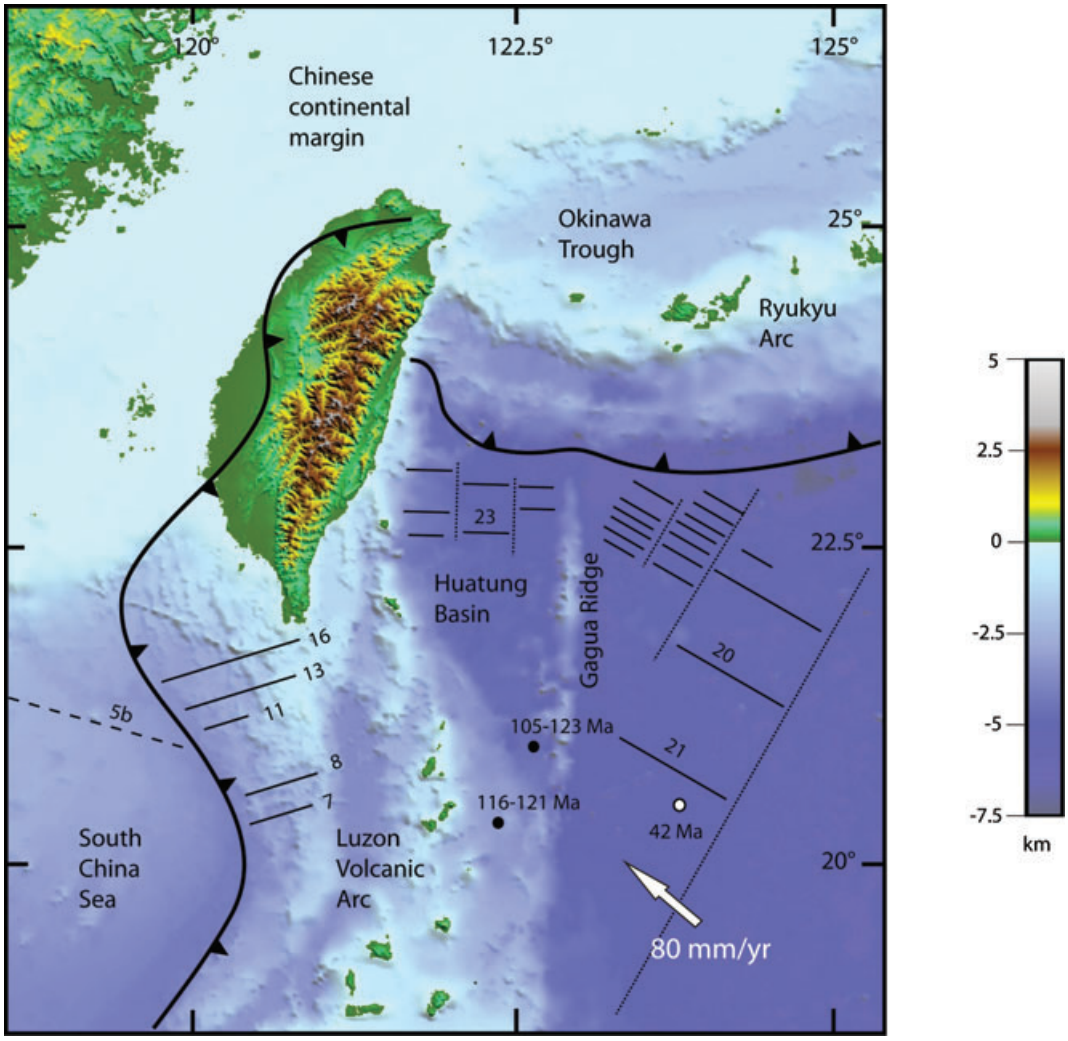

Figure 1. Geodynamic setting of the Taiwan arc–continent collision that developed in the context of two subduction zones with opposite vergence between the PSP and the Chinese continental margin. Magnetic anomalies suggest that spreading started at least 51 Ma (chron 23) in the West Philippine Basin (Huatung Basin). Dating in oceanic boreholes revealed older ages closer to 105–125 Ma (Deschamps *et al.* 2000). Eastward, the East PSP show younger ages ∼42 to 48 Ma (chron 21).

estimates between 3 and 0.9Ma (Fig. 3a). (U–Th)/He dating on zircons provides cooling ages younger than 1Ma close to AFT ages. Other constraints on peak temperatures revealed by Raman Spectroscopy of Carbonaceous Material (RSCM) techniques (Beyssac *et al.* 2008) indicate temperatures often higher than 450°C in the TS units.

The slates of the BR overlies the pre-Tertiary metamorphic basement. The BR is made of an assemblage of Eocene metasediments (Pilushan Formation), which are overlain unconformably by Miocene slates (Lushan Formation). These sediments have been metamorphosed during the ongoing collision under lower greenschist metamorphic conditions ($T = 300 \pm 50$ °C, $P = 4$ kb; Liou & Ernst 1984; Fig. 2). Reset AFT ages lower than 2 Myr, as well as reset ZFT ages younger than 3 Myr, are found in the Pilushan Formation. By contrast, the thermochronometric patterns in the Lushan Formation are more complex : partially reset or unreset AFT ages are in the range of 5.6 and 2 Myr (Fuller *et al.* 2006). Unreset samples with ZFT ages older than 30 Ma are reported together with ZFT ages younger than 3 Ma (Fig. 3a). Such FT ages have been alternatively interpreted as reset FT ages consistent with a two-stage collision (Lee *et al.* 2006). (U–Th)/He dating carried out on zircons also revealed partially reset and unreset zircons with ages ranging between 3.8 and 41 Ma (Fig. 3a). In the Pilushan slates all (U–Th)/He ages on zircons are reset with ages younger than 1 Ma. RSCM temperatures are usually lower than 350 °C.

The HR located to the west of the BR consists of Eocene–Oligocene slates metamorphosed at prehnyte–pumpellyite to lower greenschist facies ($T = 260 \pm 40$ °C, $P = 2$–3 kb; Liou & Ernst 1984). The HR is characterized by abnormally high peak RSCM temperatures locally larger than $T = 475$ °C similar to observations in the TS (Beyssac *et al.* 2007). This result is well correlated with reset AFT ages younger than 1 Ma, reset ZFT ages younger than 3 Ma and (U–Th)/He ages on zircons in the range of 1.5–2 Ma. All these data suggest a rapid exhumation of a minimum of 15 km (Beyssac *et al.* 2007). To explain such abnormal patterns, the HR can be viewed as a small-scale extensional basin originated in the rifted Chinese margin, which was subsequently inverted during the Penglai orogeny (Teng 1992; Clarck *et al.* 1993; Lee *et al.* 1997). In any case, the metamorphic data and model P–T paths for the BS and HR suggest a simple cooling and decompression from initial P–T conditions in the Chinese passive margin (Simoes *et al.* 2007).

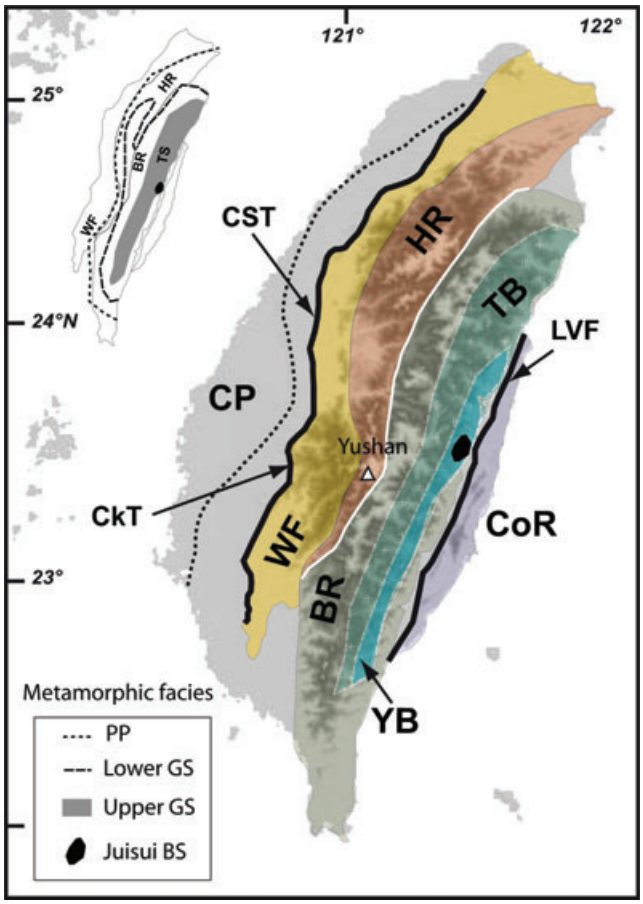

Figure 2. Simplified geological map of the Taiwan collision belt and metamorphic facies map (inset). Tectonic units are from East to West the Coastal Range (CoR), the Longitudinal Valley Fault (LVF), the Tailuko Belt (TB) and the Yuli Belt (YB) of the eastern Central Range, including the Juisui blueschist rocks, the Backbone Range (BR), the Hsuehshan Range (HR), the Western Foothills (WF) and the Coastal Plain (CP). The thick black lines depict the two main kinematic boundaries (reverse faults) accommodating the current plate convergence. They are the LVF to the East and the Chukou Thrust (CkT)-Chelungpu–Sani Thrust (CST) at the front. The white thin line corresponds to the Lishan Fault, a crustal scale backthrust that likely acted as a major faulted boundary accommodating the exhumation of the HR. Metamorphic facies map after Chen *et al.* (1983). GS, greenschist metamorphic facies; PP, prehnyte-pumpellyite metamorphic facies; BS, blueschist metamorphic facies.

Where thermochronometric constraints exist, the western foreland fold–thrust belt appears mostly characterized by unreset AFT, ZFT and ZHe ages. This is in agreement with the limited burial recorded by the outer frontal WF rocks. The highest metamorphic grades reported inner WF reveals prehnyte–pumpellyite conditions ($T = 150\ ^{\circ}$C, $P = 1$–2 kb; Liou & Ernst 1984).

2.3 Structural styles, finite strain and ductile fabrics

Crustal shortening across the whole Taiwan orogen has been first estimated to be 160–200 km (Suppe 1981). Based on modelling of foreland basin deposition patterns and age constraints on frontal thrusts, a shortening rate of 39–45 mm yr^{-1} over the past 2 Myr have been recently proposed (Simoes & Avouac 2006), consistently suggesting crustal shortening of 195–225 km over the past 5 Myr. Across the WF, finite shortening is greatly dependent on the importance assumed for basement-involved deformation with respect to thin-skinned style of deformation (Mouthereau & Lacombe 2006). Nevertheless, finite shortening in the WF should range between 15–20 km, increasing up to, for example, 42 km if thin-skinned deformation prevailed (Yue *et al.* 2005). Deformation in the HR is characterized by vertical folding in association with a pervasive steeply dipping pressure solution cleavage S1. By contrast, the BR is characterized by inclined folds in association with S1 dipping slightly to the SE. Studies on the finite ductile strain in the slate belt suggest that the HR was dominated by coaxial strain history and pure shear (Tillmann & Byrne 1995) with 130 to 450 per cent of vertical elongation (Fisher *et al.* 2002). By contrast, the BR shows top-to-the-west shear with an eastward-increasing magnitude of elongation from 40 to up to 460 per cent near the contact with the TS. The magnitude of ductile strain in the HR is low if compared with that predicted by thin-skinned critical wedge model (Clarck *et al.* 1993). This finding can be interpreted as the result of strain localization along out-of-sequence thrusts (Clark *et al.* 1993) or underplating (Simoes & Avouac 2007; Beyssac *et al.* 2007). The pre-Tertiary basement is also dominated by a single, penetrative fabric, S1, oriented NE and moderately dipping stretching lineation L1. In granitic gneiss (Chipan gneiss) L1 is defined by biotite, white mica and elongated quartz and by chlorite, actinolite, biotite and rarely white mica in metavolcanic phyllites. This penetrative fabric L1 is defined by greenschist minerals assemblage interpreted to be related to the Penglai orogeny (e.g. Lo & Onstott 1995). Taking into account the lack of evidence for prograde greenschist metamorphism, as mentioned in above section, we infer that the observed penetrative foliations that characterize the higher grade rocks in Taiwan are essentially post-peak metamorphism (i.e. retrograde). Kinematic analysis of the deformation associated with L1 is interpreted as related to lateral viscous extrusion of the TS between the slate belt and the CoR (Pulver *et al.* 2002).

2.4 Present-day kinematics

GPS velocity field derived from 1990–1995 geodetic surveys (Fig. 4) reveals that the current plate convergence is accommodated essentially across the LVF to the east and across the western frontal thrusts of the WF in agreement with the location of main active faults. In detail, shortening rates of 27–45 mm yr^{-1} are recorded across the LVF, over this period (Yu *et al.* 1997). Westward, the Central Range (BR and TS) shows a striking lack of shortening associated with a lack of seismicity (Fig. 4). The second kinematic boundary lies in the WF, where geodetic observations indicate interseismic shortening rates in the range of 4.6–27 mm yr^{-1}, across the frontal Chukou Fault (Fig. 4). On the other hand, northward, as a consequence of the Chichi earthquake, geodetic displacements in the hangingwall of the Chelungpu Thrust, still remain high with velocities of 30–45 mm yr^{-1} (Hu J.C. personal communication) but without significant modification of the first-order kinematic patterns.

2.5 Exhumation, erosion rates and heat flow

The number of available thermochronometric constraints yields quantitative estimates of the exhumation rates. For instance, on the basis of the locations of reset and unreset zones for apatite and zircon Willett *et al.* (2003) calculated erosion/exhumation rates in the range of 3–6 mm yr^{-1} in the eastern Central Range and 1.5–2.5 mm yr^{-1} in the western Central Range since ∼1 Myr. Based on assumptions for the geothermal gradient and comparison of AFT and ZFT ages, Lee *et al.* (2006) suggested a two-stage exhumation

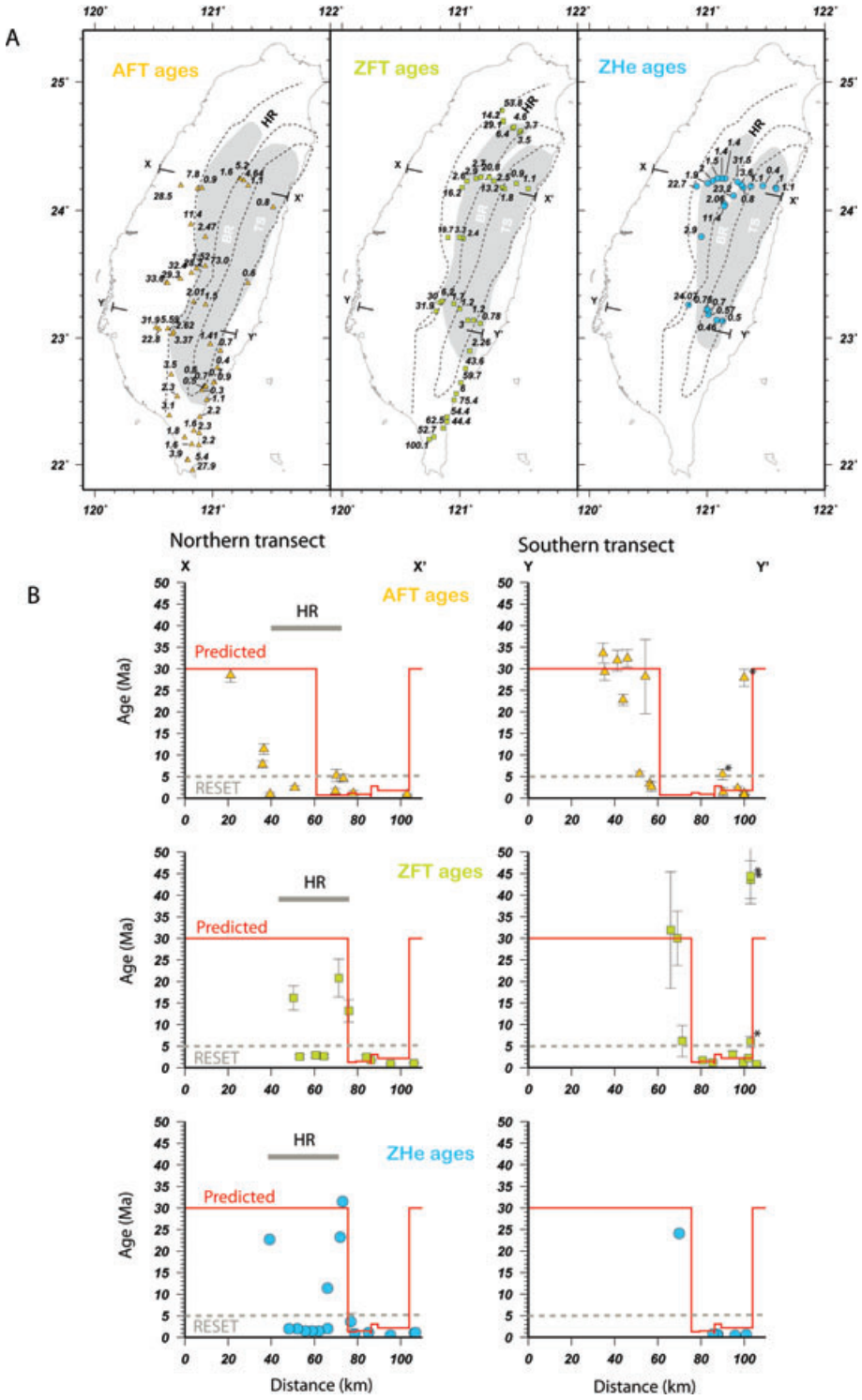

Figure 3. (a) Synthesis of thermochronometric constraints. FT ages are after compilation published in Fuller *et al.* (2006) and ZHe ages after Beyssac *et al.* (2007). Grey shading indicates inferred reset region for the studied low thermochronometer (same as Fuller *et al.* 2006 for AFT and ZFT ages). (b) Projection of observed AFT, ZFT and ZHe ages and model ages (red line) along northern and southern transects located in (a).

with low rates <1 mm yr^{-1} between 6–1 Ma followed by a rapid exhumation of 4–10 mm yr^{-1}.

Current erosion rates estimated using suspended sediments are about 3.9–5.2 mm yr^{-1} (Dadson *et al.* 2003) in agreement with former studies on stream load measurements (Li 1976), uplifted Holocene reefs and marine terraces (Peng *et al.* 1977). In addition to these constraints, fluxes of sediments supplied to the ocean have been estimated to be up to 500 Mt yr^{-1} (Dadson *et al.* 2003). They also showed that the mean annual suspended load of major rivers is strongly asymmetric across Taiwan as fluxes of erosion on the eastern slope of the orogen are 2 to 3.5 times higher than fluxes estimated from the western rivers.

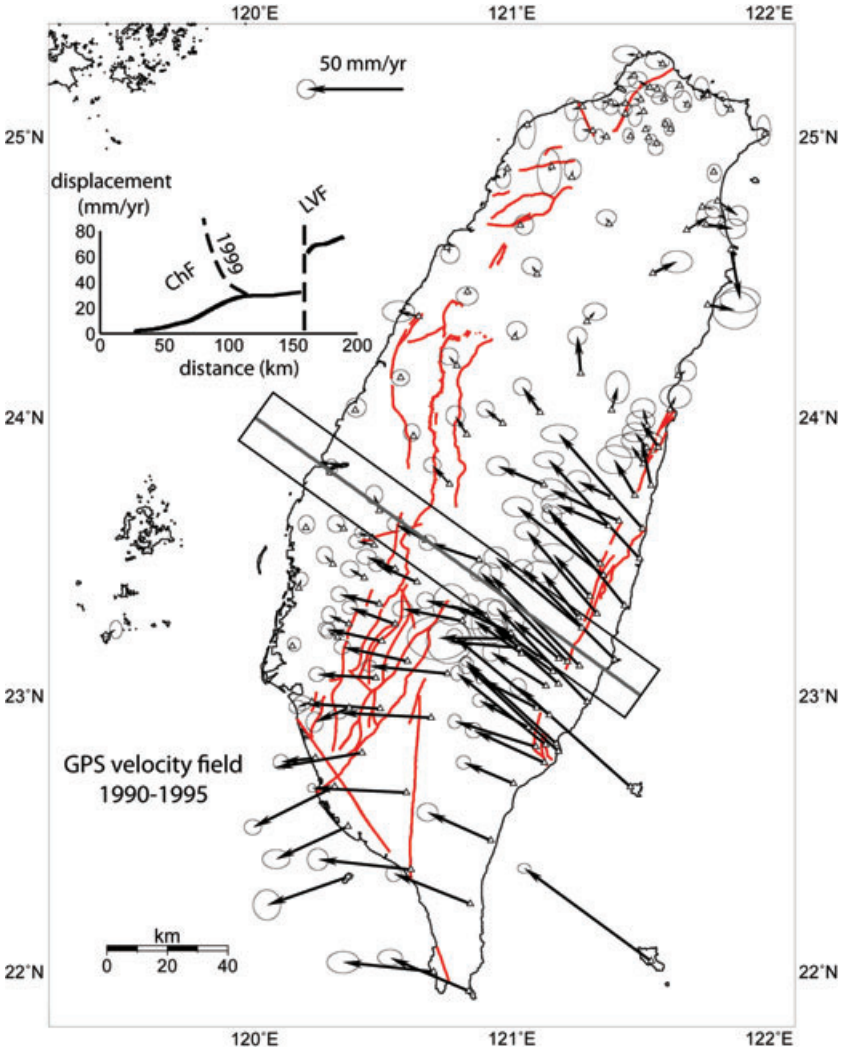

Figure 4. Present-day velocity field based on 1990–1995 geodetic surveys (after Yu *et al*. 1997). Red lines correspond to major known active faults. Horizontal geodetic velocities are plotted in cross-section (inset). The position of the main kinematic boundaries including the Longitudinal Valley Fault (LVF) and the Chelungpu–Sani Fault (ChF) are shown. Dashed lines show the departure from the 1990–1995 displacement field (solid line) that occurred in response to the activity of the ChF during the 1999 Chichi earthquake. Note that displacements are nearly constant through the Central Range, suggesting a lack of shortening in this region.

Heat flux values are characterized by maximum values of 150 mW m^{-2} in the Central Range, bounded by lower values of 50–70 mW m^{-2} in the western foreland and 70–100 mW m^{-2} to the east (Fig. 5). It is worth noting that the highest heat flux values mimic a dome-like feature centred in the Central Range. This suggests that rocks with high metamorphic grades are currently exhumed in the Central Range leading to upward deflection of the isotherms and hence local increase of heat flow.

3 A THERMODYNAMICALLY COUPLED THERMOMECHANICAL APPROACH

We have shown in the introduction that published numerical and analogue models of Taiwan had several limitations. Furthermore, the increasing number of geological and geophysical informations on the Taiwan orogen requires the use of more suitable lithospheric models that aim to account for the wide range of observations at a lithosphere scale. In this study we adopt the viscous-elastic–plastic thermomechanical numerical code PARA(O)VOZ (Poliakov *et al.* 1993) based on the FLAC (Fast Lagrangian Analysis of Continua) algorithm (Cundall 1989).

Compared to the previous versions, the code used for this study is thermodynamically coupled using THERIAK algorithm (De Capitani 1994) that evaluates equilibrium mineralogical phases and their densities as function of *P–T* conditions computed by the thermomechanical kernel of PARA(O)VOZ. The new densities and physical properties are dynamically re-integrated back to the thermomechanical kernel.

This thermomechanical kernel solves simultaneously the Newtonian equations of motion

$$\frac{\rho \partial v_i}{\partial t} - \frac{\partial \sigma_{ij}}{\partial x_j} - \rho g_i = 0, \tag{1}$$

$$\frac{D\sigma}{Dt} = F(\sigma, u, \nabla u, \ldots T \ldots), \tag{2}$$

and the heat transfer equation

$$k.\mathrm{div}(\nabla T) - \rho C_p \frac{\partial T}{\partial t} + H_r = \mathrm{v}\nabla \mathrm{T}, \tag{3}$$

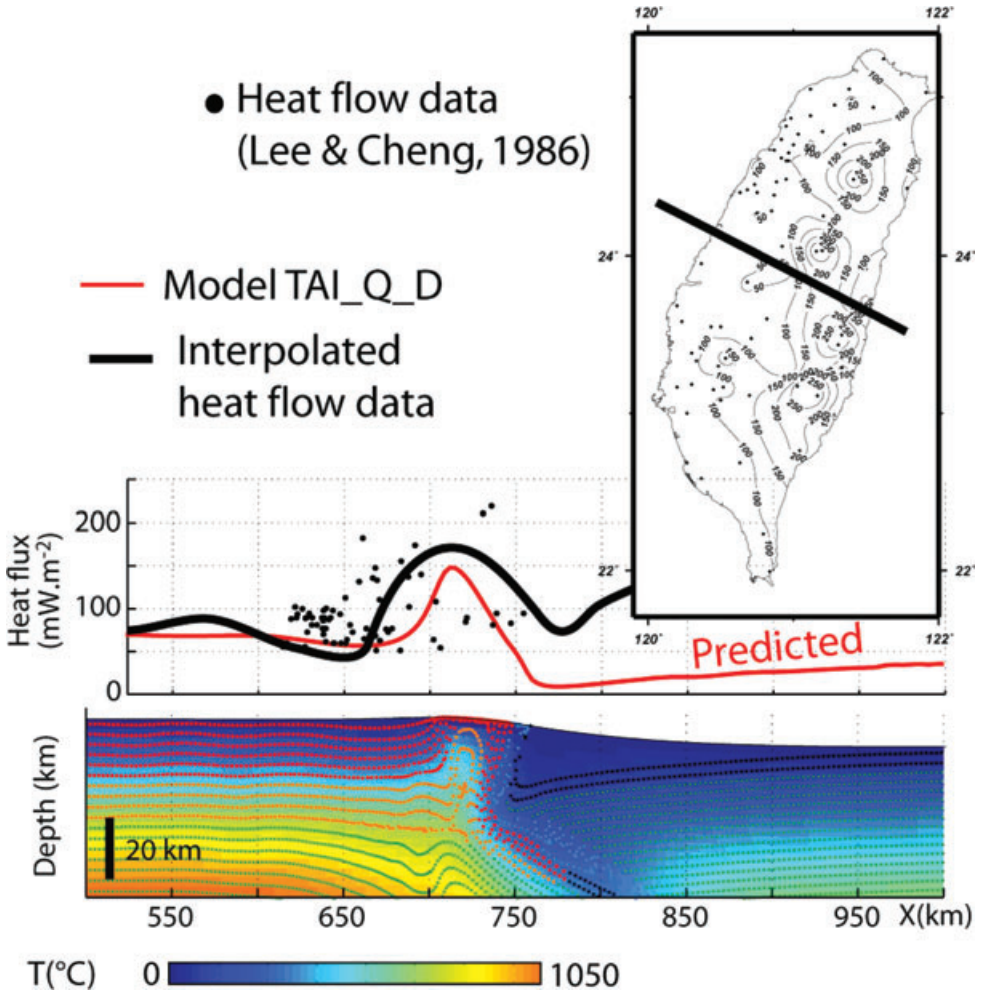

Figure 5. Comparison between observed (interpolated) heat flow data (Lee & Cheng 1986) and heat flow predicted in our preferred model Tai_Q_D (after 5 Myr of the numerical experiment). Spatial distribution of interpolated heat flow data (black thick solid line) is shown on map in the upper right inset. They are projected along NW–SE directed profile for comparison. Heat flow values larger than 300 mW m^{-2} and lower than 50 mW m^{-2} were excluded from this analysis because of the possible interference of geothermal circulation and groundwater movement (Lee & Cheng 1986).

in a large-strain Lagrangian formulation using Jauman's corrections for rotation of principal stress axis.

In eqs. 1–3 **u** is the displacement vector, **v** is velocity, ρ is density, t is time, g is the acceleration due to gravity, D is material objective derivative, σ is Lagrangian stress, T is temperature, C_p is the specific heat, k is the thermal conductivity and H_r is the internal heat production per unit volume. F denotes functional relationship for viscous-elastic–plastic constitutive law. We use Mohr–Coulomb criterion for plasticity and a non-linear power law for viscous flow.

The upper surface in all models is kept free and is additionally affected by erosion–sedimentation processes modelled with a diffusion law

$$\frac{\partial h}{\partial t} - \nabla(k_{\text{ero}}\nabla h) = 0, \tag{4}$$

where h, t and k_{ero} correspond to topography, time and coefficient of erosion, respectively.

The time-step for solving all these equations is of the order of 10 yr (Such a high resolution in time allows to handle all possible instabilities and non-linearities associated with complex rheologies and phase changes). Because it allows for large deformation it is particularly suitable for modelling long-term geological deformation at the lithospheric scale.

For our study, the thermomechanical code is thermodynamically coupled with the THERIAK algorithm (De Capitani 1994) back to the thermomechanical kernel to reproduce the changes in rocks density and thermal expansion/contraction, associated in particular with the eclogitization. THERIAK relies on the free energy minimization. To save computation time, the density field is pre-computed at the beginning of the computations for several typical bulk chemical compositions (see Yamato *et al.* 2007 for further details). Passive markers are incorporated within each grid cell of the model to track *P–T–z*-shortening histories of rocks and to improve the remeshing procedure (Yamato *et al.* 2007). Such markers enable us, for example, to track the thermal evolution of a given rock particle during deformation and hence allows for prediction of thermochronometric ages. In the same way, *P–T–t* paths can be computed. Owing to the particle-in-cell technique, local horizontal shortening rates and exhumation rates are traced during the computations. This allows us to study the long- and the short-term deformation distribution across the Taiwan orogen and to compare it with the geological data. The overall advantages of the numerical approach used is that it allows us to test a large number of parameters controlling the Taiwan orogen including erosion rates, crustal rheologies or convergence rates can be tested.

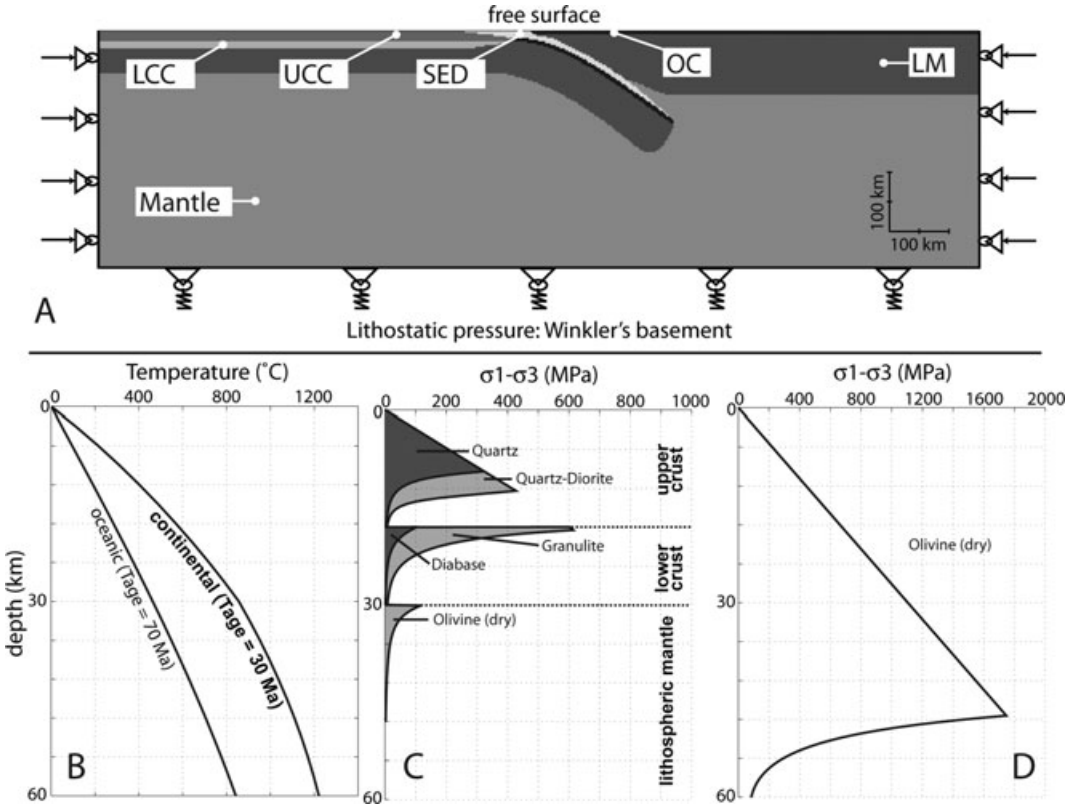

Figure 6. Model setup for all studied numerical experiments. (a) Initial plate geometry and boundary conditions applied on the model box. Abbreviations: LCC, lower continental crust; UCC, upper continental crust; SED, sediments; OC, oceanic crust; LM, lithospheric mantle. (b) Thermal profiles for the oceanic lithosphere of the PSP (thermal age is 70 Ma) and the continental lithosphere of the Chinese margin (thermal age is 30 Ma). (c) Yield strength envelopes computed for the thermal profiles in (b) for different composition of the continental crust used in the present study. (d) Yield strength envelope for the oceanic lithosphere.

Inside the model, all motions of material are free (i.e. there is no pre-imposed 'S' points or any internal forcing on solution). The free upper surface of the model is submitted to erosion/sedimentation tuned to the averaged values specific to the area. At the bottom of the model we apply Winkler's pliable basement condition, which corresponds to hydrostatic equilibrium with the underlying deep low-viscosity mantle assuming a small density contrast (10 kg m^{-3}).

We do not provide a more detailed description of PARA(O)VOZ algorithm because this is was already done in a number of recent publications (Burov *et al.* 2001; Le Pourhiet *et al.* 2004; Toussaint *et al.* 2004a,b; Yamato *et al.* 2007).

3.1 Boundary conditions

The boundary conditions refer to the common collision model setups used in previous studies (Burov *et al.* 2001; Toussaint *et al.* 2004a,b; Burov & Yamato 2007; Burov & Toussaint 2007; Yamato *et al.* 2007, 2008). The only boundary condition that is fixed in all numerical experiments is the plate velocity applied at both lateral sides of the model box. The velocities are dependent on the rate of convergence averaged since the beginning of the model, that is, since the beginning of the collision. In this respect, the convergence of the PSP relative to Eurasia is assumed to be 50 km Myr^{-1} to match the magnetic lineations in the Huatung Basin and below the Manila accretionary prism 15 Ma (chron 5b; Sibuet *et al.* 2002). The total convergence rate is divided into half velocities of 25 km Myr^{-1} applied on both sides of the model. The application of the total convergence rate on the left or the right border does not modify the model results.

3.2 Initial plate configuration

The initial plate configuration (Fig. 6a) refers to the time at which the Eurasian continental margin is supposed to initiate its subduction beneath the PSP in the Late Miocene. At this stage, the thinned continental lithosphere is attached to the oceanic lithosphere of the South China Sea and the initial dip angle of the oceanic slab is fixed at 30° in agreement with the average dips of current oceanic subduction slabs worldwide (see compilation by Cruciani *et al.* (2005)). It is worth noting that the continental margin has not yet been subducted and the continental slab is then assumed to be horizontal. This is a major difference with kinematic models in which an initial dip angle for the continental crust is fixed thus forcing the subduction of the continent.

Several lines of evidence, including the age of volcanism in the CoR and plate reconstruction, suggest that the E-directed subduction did not start before 15 Ma (Sibuet *et al.* 2002) of the collision considered to be between 9 and 6 Ma (Lin *et al.* 2003; Tensi *et al.* 2006). We thus infer that the oceanic subduction lasted 6 Ma before collision occurred (Sibuet & Hsu 2004). Given a fixed convergence rate of 50 km Myr^{-1} and uncertainties on the initiation of both the oceanic subduction and continental collision we have estimated the length of the oceanic slab to be 300 km.

In all numerical experiments presented in this study, the initial size of the 'model box' is 1482 km in length and 399 km in depth

with a spatial resolution (meshing) of 3 × 3 km. In each mesh of the model, 4 markers were added at the nodes of each element, 1 at the barycentre of the element and 4 at the barycentre of the four subtriangles constituting the element. The mineralogical compositions used for the calculation of the density of each material in the model correspond to commonly referred compositions, that is, composition of granite, MORB basalt, pelite and mantle for continental crust, oceanic crust, sediments and mantle, respectively (see Yamato *et al.* 2007 and references therein for further details).

The thickness of the continental crust is set to 30 km in agreement with geophysical data in the foreland (Rau & Wu 1995; Ma & Song 1997; Yen *et al.* 1998). The continental crust is believed to be rheologically layered; hence we have subdivided the crust into an upper (mainly brittle) continental crust and a lower (mainly viscous) crust (Fig. 6c) both *P*–*T*-dependent following the rheological parameters presented in Table 2. Based on the depth-distribution of seismicity and former rheological modelling of the Chinese margin (Mouthereau & Petit 2003) we set the thickness of the upper seismogenic crust having pressure-dependent rheology to 18 km. The remainder, that is, 12-km-thick layer corresponds to the viscous and nearly aseismic lower crust (Table 1). The thermomechanical characteristics of these two parts depend on the mineralogy considered for these two layers as detailed below and in Table 2.

3.3 Initial geotherm

The initial geotherm (Fig. 6b) is computed from plate-cooling models for oceanic (Parsons & Sclater 1977; Turcotte & Schubert 2002) and continental lithosphere (Burov & Diament 1995; Parsons & Sclater 1977) and consistent with the thermal (cooling) ages of both the oceanic and the continental lithospheres. The procedure used for computation of initial thermal structure is described in further details in Yamato *et al.* (2008). The thermal parameters are presented in Table 2. Thermal ages are defined by the last thermal event at which the plate cooling initiated. The thermal age of the PSP is constrained by geophysical studies and boreholes of the oceanic basement below the Huatung Basin (Deschamps *et al.* 2000). Magnetic anomalies suggest that spreading started at least ∼51 Ma (chron 23) in the northern Huatung Basin (Fig. 1). However, in the southern Huatung Basin dating of the oceanic floor using boreholes revealed older ages closer to 105–125 Ma (Fig. 2). Eastward, the East PSP show younger ages ∼42 to 48 Ma (chron 21). We hence adopt an average age of 70 Ma. For the continental part, the thermal structure (multilayer cooling half-space) is defined by setting its thermal age to 30 Ma (Fig. 6b) in agreement with the initiation of spreading in the South China Sea (Taylor & Hayes 1980; Lee & Lawver 1995). Figs 6(b)–(d) clearly show that the lithospheric mantle of the PSP is colder and stronger than the Eurasian margin. The first-order rheological contrast between both plates is a key parameter that constrains the development of the Taiwan mountain belt and the final geometry of the collision.

3.4 Rheological parameters

Viscous creep parameters of all model materials are presented in Table 2. PARA(O)VOZ code uses viscous-elastic–plastic rheologies, for description of each of which a total of seven material parameters are needed: three parameters for the viscous behaviour (n, A and E), two parameters for the elastic behaviour (the Lamé's coefficients λ and μ) and two parameters for the plastic law (cohesion Co and frictional angle ϕ). The values of elastic parameters (Table 1) were chosen assuming a lithosphere with a Poisson's ratio constant equal to 0.25 (which is equivalent to $\lambda = \mu$). For plastic behaviour, a frictional angle of 30° is considered for all crustal rocks according to Byerlee's law (Byerlee 1978). Cohesion values only differ for surface rocks. Although the elastic and plastic parameters of rocks are fairly well known, creep parameters used in the viscous law are less well constrained (e.g. Watts & Burov 2003). In our study, we have tested several material creep parameters in the crust that are presented in Table 2.

Table 1. Thermomechanical coefficients and boundary conditions used in our models.

Physical parameters	
All rocks	$\rho = f(P,T)$ calculated using Theriak (kg m^{-3})
	Friction angle = 30°
Upper continental crust (UCC)	Material: Quartz∗
	Thermal conductivity: 2.5 W m^{-1} °C^{-1}
	Thermal diffusivity: 8.3 × 10^{-7} m^2 s^{-1}
	Lamé constants: $\lambda = \mu = 3 \times 10^{10}$ Pa
	Cohesion: 20 x 10^6 Pa
Lower continental crust (LCC)	Material: Diabase∗
	Thermal conductivity: 2.5 W m^{-1} °C^{-1}
	Thermal diffusivity: 6.7 × 10^{-7} m^2 s^{-1}
	Lamé constants: $\lambda = \mu = 3 \times 10^{10}$ Pa
	Cohesion: 20 × 10^6 Pa
Sediments (SED)	Material: Quartz∗
	Thermal conductivity: 2 W m^{-1} °C^{-1}
	Thermal diffusivity: 8.3 × 10^{-7} m^2 s^{-1}
	Lamé constants: $\lambda = \mu = 1 \times 10^{10}$ Pa
	Cohesion: 1 × 10^6 Pa
Oceanic crust (OC)	Material: Olivine∗
	Thermal conductivity: 3.5 W m^{-1} °C^{-1}
	Thermal diffusivity: 8.75 × 10^{-7} m^2 s^{-1}
	Lamé constants: $\lambda = \mu = 3 \times 10^{10}$ Pa
	Cohesion: 20 × 10^6 Pa
Mantle	Material: Olivine∗
	Thermal conductivity: 3.5 W m^{-1} °C^{-1}
	Thermal diffusivity: 8.75 × 10^{-7} m^2 s^{-1}
	Lamé constants: $\lambda = \mu = 4 \times 10^{10}$ Pa
	Cohesion: 300 × 10^6 Pa
Thermal parameters	
*T*s; *T*hl	0 °C; 1330 °C
hl∗	120 km
Cont. *T*age∗	30 Ma
Oc. *T*age∗	70 Ma
hr, *H*c	10 km, 1.10^{-9} W kg^{-1}
Other parameters	
Huc	18 km
Hlc	12 km
keros∗	5000 m^2 yr^{-1}
Conv. rates∗	50 mm yr^{-1}

Note: Parameters presented with '∗' constitute those used in the reference numerical experiment (Tai_Q_D). They have been submitted to a parametric study presented in Table 3. For physical parameters section, abbreviations are similar to those presented in Fig. 3. *T*s and *T*hl correspond to the temperature at the surface and at the bottom of the continental lithosphere (hl), respectively. Thermal ages (*T*age) used to calculate the temperature profile for the continental lithosphere (Cont.) and the oceanic lithosphere (Oc.) are also reported. Concerning radiogenic heating, hr, corresponds to the decay depth where radiogenic heating is activated (only in the continental crust material) and *H*c is the value of the radiogenic production. *H*uc the thickness of the upper continental crust and *H*lc the thickness of the lower continental lithosphere are from (Mouthereau & Petit 2003); *k*eros is the coefficient of erosion; *Conv. rates*, Total convergence rate applied on our model.

Table 2. Creep parameters used in this study.

	n	A (MPa^{-n} s^{-1})	E ($J\ mol^{-1}$)
Quartz∗	3	6.8×10^{-6}	1.56×10^5
Diabase∗	3.05	6.3×10^{-2}	2.76×10^5
Quartz-Diorite	2.4	3.01×10^{-2}	2.12×10^5
Mafic granulite	4.2	1.39×10^4	4.45×10^5
Olivine (dry) ∗	3	7×10^4	5.10×10^5

Note: Parameters presented with '∗' constitute those used in the reference numerical experiment (Tai_Q_D). Creep parameters data sources are from Ranalli & Murphy (1987) for quartz, Carter & Tsenn (1987) for diabase, Goetze (1978), Hansen & Carter (1982) and Wilks & Carter (1990) for quartz-diorite, mafic granulite and dry-olivine, respectively.

The Palaeogene sedimentary cover deposited onto the Chinese margin is included as part of the upper crust with the same rheological parameters. So the model inhibits the development of shallow low-dipping zone of weakness in the Chinese margin and thus decoupling in the shallow crust. This approach is validated *a posteriori* since deformation pattern are controlled, to first order, by the contrast of rheology between the upper and the lower crust.

4 MODEL RESULTS

From the examination of performed calculation runs we conclude that only the model Tai_Q_D is in good agreement with natural observations (Fig. 7). To demonstrate why this model is preferred we first present a full comparison between its predictions and natural observations. Then, the results of parameters variations are presented to identify the critical parameters of the reference model (see Table 3 and Section 6).

In this reference numerical experiment, quartz and diabase composition has been adopted for the upper and the lower crust, respectively. The average erosion coefficient, used in the diffusion equation (4) that simulates erosion, is 5000 $m^2\ yr^{-1}$. The age of the collision corresponding to the duration of the model is estimated to be 5 Myr, which is roughly in agreement with ages currently considered for Taiwan collision on the basis of stratigraphic studies and modelling of the basin subsidence in the western foreland basin (Teng 1990; Lin *et al.* 2003; Tensi *et al.* 2006).

4.1 Main tectonic features

4.1.1 Taiwan accretionary wedge

In this section, we summarize the main characteristic features of the collision model at the end of the numerical experiment. The contraction of the Chinese crust has led to the development of a typical collision wedge. The accretion of the Asian crust is accommodated by the decoupling in the lower crust and the westward nearly rigid displacement of the oceanic lithosphere. Strain rates clearly highlight the localization of the main decollements and other major shear zones within the collision belt (inset of Fig. 8a). The main PSP/EUR decoupling follows the moderately east-dipping subduction panel, then it flattens westward at the base of the orogenic wedge at a depth of ∼25 km and finally ramps up to the surface along a 40°-dipping frontal thrust. In the footwall of this frontal ramp, that is, below the western foreland, strain rates reveal that compressive deformation still remains significant especially in the lower crust and across rheological boundaries in the mid-crust and at the Moho.

Deformation within the orogenic wedge is remarkably dominated by the large-scale folding of the Asian crust controlled by the viscous thickening in the lower crust (Figs 7 and 8). This mechanism could be mistaken for underplating as proposed in recent models of Taiwan (Barr & Dahlen 1989; Simoes & Avouac 2006; Beyssac *et al.* 2007; Simoes *et al.* 2007). However, instead of being related to duplexing where the décollement is stepping down, the predicted upward advection of Asian material is rather the consequence of frontal accretion and viscous thickening of the incoming Asian lower crust. Such a frontal accretion of nearly the whole crust is well depicted by the model velocity field (Fig. 9). In addition, the exhumation at the rear of the wedge is permitted by the erosion and backthrusting. As a consequence, HT isotherms are deflected upward uplifting rocks that experienced greenschist and amphibole metamorphism.

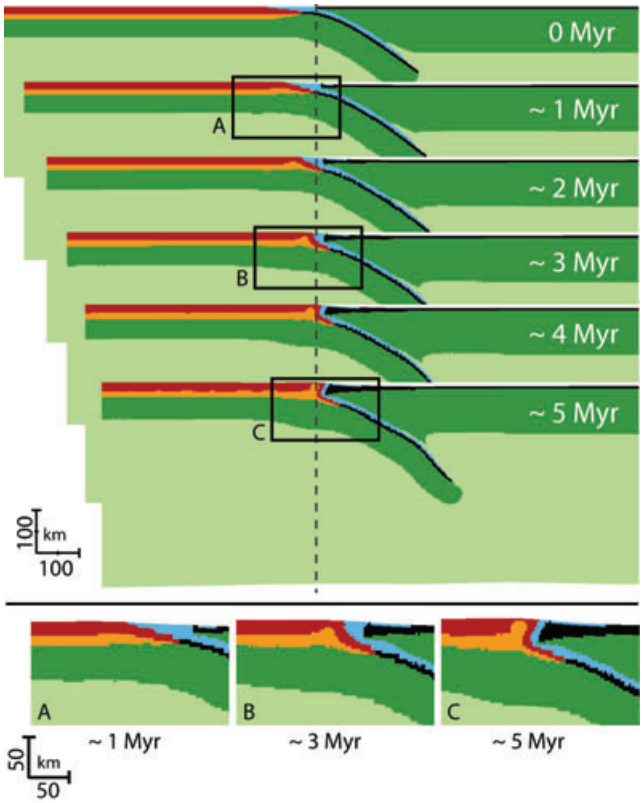

Figure 7. General evolution of the plate configuration during 5 Myr for the reference model (Tai_Q_D). The stage at 5 Myr (inset c) is believed to correspond to the present-day configuration. Note that as the Eurasian plate indents the PSP, the initial plate suture is moving toward the upper plate. Since no new passive markers are introduced, meshes of newly deposited sediments are stretched leading to increase artificially the thickness of the crust of the PSP. Black meshes should be viewed as a mix of sediments and oceanic crust rather than oceanic crust only.

4.1.2 The Philippines Sea Plate

The deflection of the PSP is clearly depicted on the eastern side of the model (Figs 7 and 8b). It is outlined by the development of a retro-foreland basin filled by synorogenic deposits eroded from the eastern side of the orogen. Such a deflection is likely caused by both the topographic loading arising from the mountain building and the intrinsic negative buoyancy of the PSP. The plate boundary, which is assumed to be represented by the Longitudinal Valley Fault, lies along the former Miocene oceanic accretionary wedge in a transitional area squeezed between the deformed PSP and the rapidly

Table 3. Parametric study.

Name of the numerical experiment	conv. rate (mm yr^{-1})	k_{eros} (m^2 yr^{-1})	Continental material Upper crust	Lower crust	Cooling/ exhumation.	PT	HF	Erosion/ Sediment.
Reference experiment								
Tai_Q_D (reference)	50	5000	Q	D	+	+	+	+
Influence of the erosion								
Tai_eros-	50	2500	Q	D	-	-	-	-
Influence of the convergence rate								
Tai_V+	100	5000	Q	D	-	-	-	-
Tai_V–	25	5000	Q	D				
Influence of the rheology								
Tai_QD_MG	50	5000	QD	MG	-	-	-	-
Tai_QD_D	50	5000	QD	D	-	-	-	-
Tai_Q_MG	50	5000	Q	MG	-	-	-	-

Numerical experiments for which the sensitivity to model parameters has been tested. Abbreviations: conv. rate, total convergence rate; k_{eros}, erosion coefficient used in the diffusion law; Q, quartz; D, diabase; QD, quartz-diorite; MG, mafic granulite. Modified parameters are shown with bold characters. ± signs refers to successful/unsuccessful reproduction of observations such as cooling/exhumation, *P–T* conditions (*PT*), Heat Flux (HF) and Erosion/sedimentation.

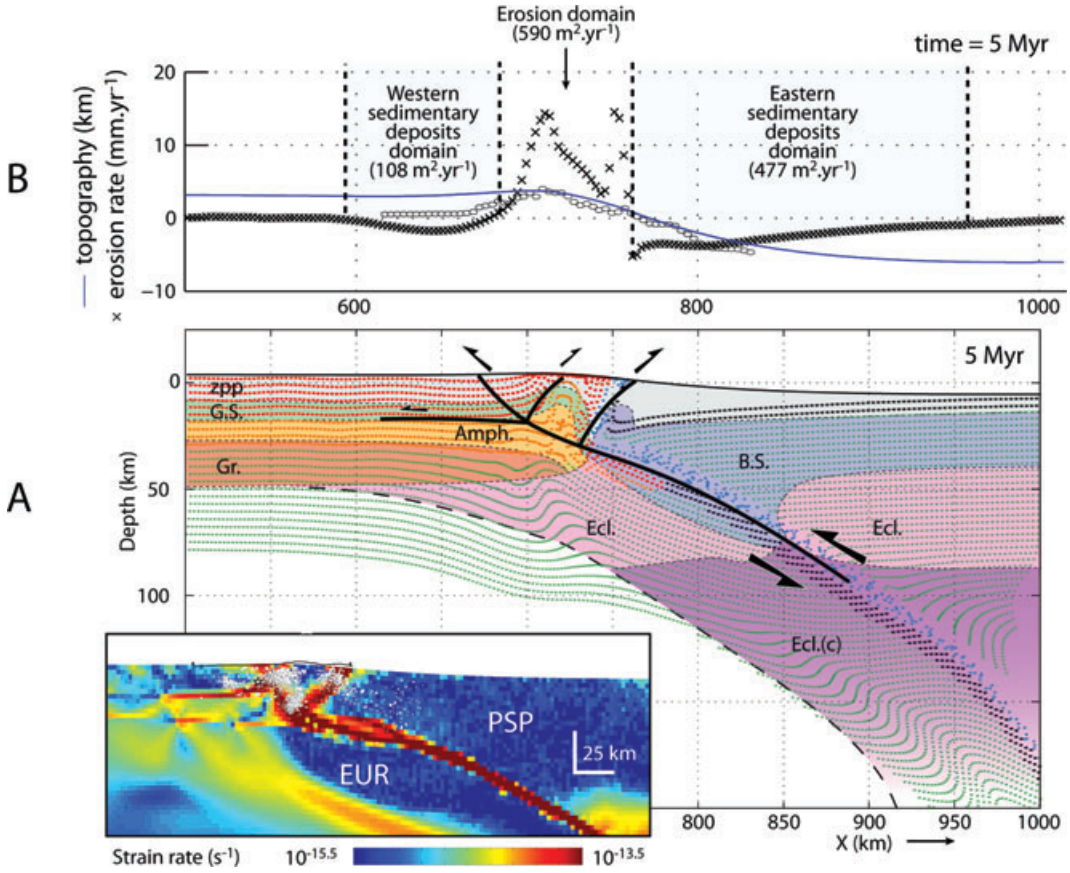

Figure 8. Detailed view of the reference model (Tai_Q_D) at the end of the model run, which corresponds to inset (c) of Fig. 7. Metamorphic facies zones presented in (a) are calculated from the *P–T* conditions at final stage at 5 Myr. For instance, no eclogitization is recorded in the lower crust of the Chinese margin beneath the Taiwan mountain belt. Location and motions along major fault zones are deduced from strain rates in the lower left-hand inset. Note that the strain rates distribution indicates that the lower crust can potentially release strain at fast rates and thus is able to produce earthquakes. Abbreviation: Amph., amphibolite facies; B.S., blueschist facies; Ecl., eclogite facies; Ecl.(c), eclogite with coesite; Gr., granulite facies; G.S., greenschist facies; zpp, zeolithe-prehnyte-pumpellyite facies. (b) Predicted (blue line) and observed topography (white dots). Erosion rates (and eroded/deposited areas) as well as erosion/sedimentation fluxes are calculated over the last computed increment of deformation and is equivalent to the current erosion rates.

uplifted collision wedge. At the end of the numerical experiment, this fault boundary, initially East-dipping, has rotated from its original position to become an east-vergent 80°-dipping reverse fault at the front of the indenting PSP.

4.2 Erosion–sedimentation distribution

Erosion rates (positive) and sedimentation rates (negative) calculated for the last increment of convergence show two adjacent

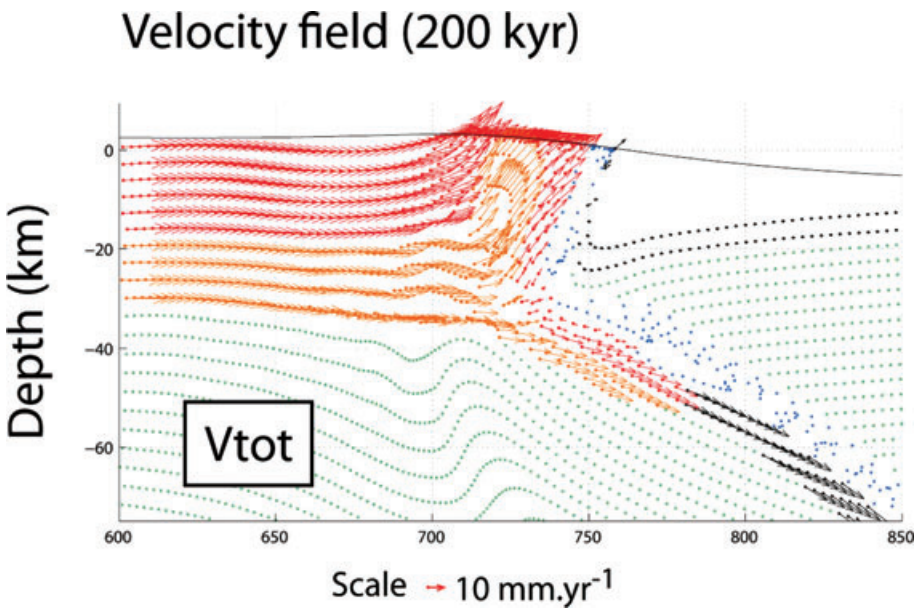

Figure 9. 2-D velocity field in the Chinese margin crust calculated over the past 200 kyr with respect to a fixed point in the PSP. Accretion of both the upper crust (red) and the lower crust (orange) is clearly depicted. Subduction of the Chinese margin can only be seen at depths deeper than 25 km beneath the suture zone (blue particles of the former accretionary prism), which is the depth of the basal shear zone observed in Fig. 5. Exhumation identified in the western frontal part of the belt results from the differential displacement between the upper and lower crustal rocks allowed by intracrustal decoupling. Exhumation at the rear results from the extrusion of the margin produced by the upward advection of lower crustal flow and shearing across the LVF.

flexural basins (Fig. 8b). Their widths are proportional to elastic thickness of plates on which they develop. Therefore the Western Foreland Basin is narrower ($\sim$ 100 km) with regard to the eastern (retro-)foreland basin ($\sim$ 180 km) since it developed on a weaker and younger plate. The sedimentation rates in the Western Foreland are about 2 mm yr^{-1} whereas in the eastern (retro-) foreland basin, sedimentation rates reach values of 3–4 mm yr^{-1} in accordance with maximum pleistocene depositional rates recorded in the West foreland basin (Lin *et al.* 2003; Tensi *et al*. 2006) and to some extent with the thick continent-derived flyschs observed in the CoR (Lundberg & Dorsey 1990; Huang *et al.* 1995). In details, except for local high values of 10 to 15 mm yr^{-1} in the vicinity of the highest mountain slopes, the erosion rates remain in the range of 3–10 mm yr^{-1}, which is in good agreement with the current erosion rates estimated based on sediment load or indirectly estimated using erosion law of FT data (Dadson *et al*. 2003, Willett *et al.* 2003). In our 2-D model, the total eroded material flux over the mountain range is estimated to be 590 m^2 yr^{-1}. 80 per cent are transported in the eastern retro-foreland basin (477 m^2 yr^{-1}) and the remainder is supplied to the Western foreland basin (108 m^2 yr^{-1}). These fluxes should be viewed as a first approximation as they do not take into consideration the 3-D plate configuration. Indeed, the development of longitudinal drainage, for example, in the western foredeep, likely removed sediments out of the plane of the section.

4.3 Heat flux

The distribution of the heat flux at the end of the modelling run is a very important constraint for evaluating our thermomechanical model in comparison to the documented thermal history and thermochronometers ages. We calculate heat flow q according to Fourier's law

$$q = -k.\frac{\mathrm{d}T}{\mathrm{d}z}, \tag{5}$$

using a thermal conductivity $k = 2.5$ W m^{-1} K^{-1} (Table 1) and determining the vertical temperature gradient dT/dz for the upper 6 km of the model.

Results are presented in Fig. 5. The spatial variations in the heat flux (Lee & Cheng 1986) are in good agreement (Fig. 5) regarding wavelengths and amplitudes. Heat flux values of 50 to 60 mW m^{-2} observed in the foreland are in good agreement with predicted heat flux of $\sim$62 mW m^{-2}. The decrease to the East of the heat flux due to the bending of the Chinese margin is also reproduced. This is followed by a sharp increase of heat flux in the central part of the orogen up to peak values of 150 mW m^{-2}, which are closer to the measurements in the eastern Central Range. One of the main characteristics of the observed heat flux is outlined by the decreasing heat flux toward the Longitudinal Valley. Our model consistently predicts lower values. However, although we predict values close to 20 mW m^{-2} on the floor of the cold PSP, observed heat fluxes are larger than 50 mW m^{-2} (Fig. 5). The apparent inconsistency between model heat flux and observation is related to the absence of the CoR in our models. Moreover, differences throughout the model may also arise from the fact that, in our models, frictional heat production was set to zero in contrast to previously presented models (e.g. Burg & Gerya 2005; Faccenda *et al.* 2008; Gerya *et al.* 2008).

5 COMPARISON OF PREDICTED AND OBSERVED DEFORMATION AND EXHUMATION PATTERNS

To better evaluate our model we have compared the long-term predicted thermochronometric ages and deformation distribution in our model with observations (see Introduction). To this aim, we have tracked eleven coloured markers having originally a regular spacing (Fig. 10). All these markers are initially located in the upper crust at the beginning of the numerical experiment. We chose

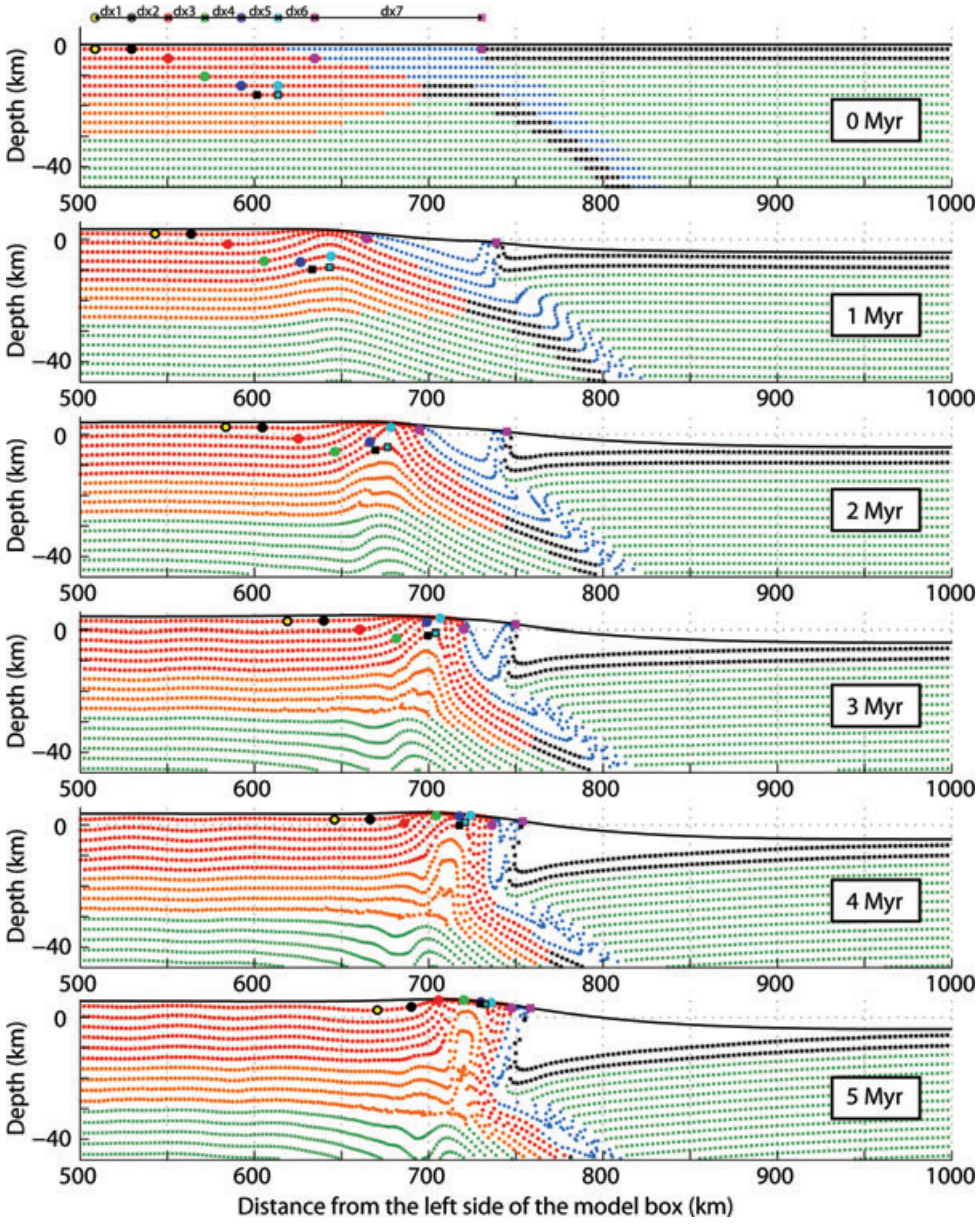

Figure 10. Close-up view of our preferred model (Tai_Q_D) in the collision area. The figure shows the evolution of the eleven markers shown as dots or squares with distinct colours. They are all located in the upper crust of the Eurasian margin and are thus consistent with a maximum exhumation of 16 km. At each time-step, we record the depth, the vertical and horizontal position, the pressure and the temperature for these markers during 5 Myr. In red, upper continental crust; orange, the lower continental crust is in orange; blue, sediments of the accretionary prism; black, oceanic crust and green, lithospheric mantle.

markers that are located close to the surface to facilitate the comparison with the present-day configuration in the Taiwan mountain belt.

5.1 Distribution of long-term and short-term shortening

We estimate that the total shortening associated with collision between Eurasia plate (yellow dot) and the PSP (magenta square) amounts to 133 km (Fig. 10). About 30 km of shortening must be added because of the deformation within the PSP (between magenta square and magenta dot). This shortening is taken up within the accretionary wedge and the weakest part of the PSP, for example, the Luzon Arc not modelled in our numerical experiment. Among these 133 km, less than half, that is, 48 km, are taken up within the Chinese continental margin. For instance, across the frontal thrusts (i.e. between yellow and red dots) our modelling predicts long-term shortening of ∼7 km amounting to 13 km if we consider deformation to the east (i.e. including the green particle). This represents 14.5 to 27 per cent of long-term deformation accommodated across the frontal part of the Taiwan mountain belt, which is fairly consistent with available constraints from cross-section balancing in the Western Foothills ranging between 10 and 30 per cent (Mouthereau *et al.* 2001; Mouthereau & Lacombe 2006). However, this result disagrees with thin-skinned interpretation of wedge deformation. We further estimate that 85 km of the total shortening, that is, 64 per cent were accommodated within the ancient oceanic wedge that currently forms the suture zone (LVF). Part of this ancient oceanic accretionary prism is now exposed in the Lichi mélange (southern CoR) and within the ophiolitic blocks exposed in the Yuli Belt including the HP-rocks exposed in the Juisui area.

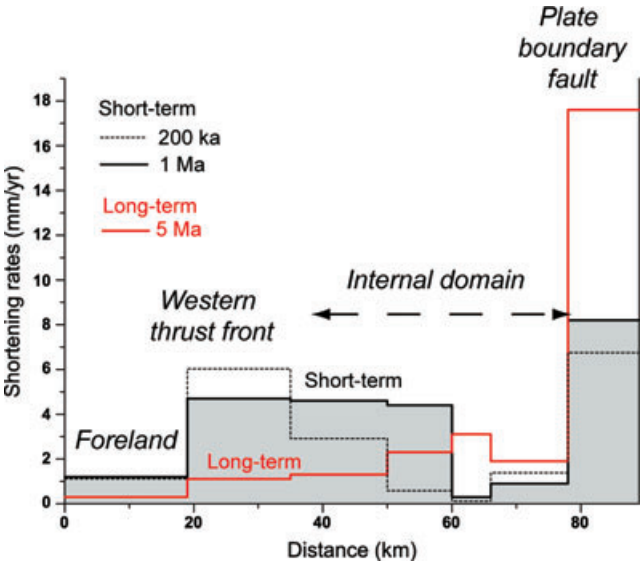

Figure 11. Long- (5 Myr) and short-term (1 Myr and 200 kyr) distribution of shortening in the reference model Tai_Q_D, calculated by considering the horizontal position of the studied particles (see Fig. 10). For instance, shortening in the foreland is assumed to represent the shortening calculated between yellow and black dots of Fig. 7. The accumulation of shortening currently recorded at the thrust front by active and seismogenic thrusting probably occurred in the past 1 Myr. This appears to be associated with a clear deficit of shortening in more internal domains. This trend seems to be more evident with the reduction of the time window considered. Note that the width W of the collision belt defined by the distance between the yellow dot and the magenta square is 89 km, which is equivalent to the present-day width of the Taiwan Island.

Fig. 11 reports both the long- and short-term shortening rates calculated in the model. The maximum long-term shortening rates of 17 km Myr^{-1} predicted by the model are located across the LVF, that is, across the suture zone. Westward, within the collision wedge, the cumulated long-term deformation reveals crustal shortening rates increasing from the front (∼1 km Myr^{-1}) to the rear of the Taiwan orogenic wedge (∼3–4 km Myr^{-1}, Fig. 11). Our model predicts a remarkable lack of shortening in a narrow domain of the most internal part of the collision belt. This narrow zone has also recorded little burial as seen in Fig. 10.

Although the rates of shortening across the wedge are of the order of rates estimated across the southern WF by cross-section balancing (Mouthereau *et al.* 2001) they appear significantly lower than the rates of shortening of 39–45 mm yr^{-1} calculated over the past 2 Myr (Simoes & Avouac 2006). We suggest that such a discrepancy might be caused by kinematic changes leading to the increase of shortening over the past 2 Myr. This possibility will be examined in the following section.

In an attempt to calibrate our preferred model with short-term geodetic deformation we have also calculated shortening rates over the last 1 Myr and 200 kyr (Fig. 11). Prior to comparison between predictions and observations it appears necessary to modify the short-term rates of deformation predicted by the modelling. Indeed, the geodesy (see Fig. 4) shows that the present-day plate convergence is 80 km Myr^{-1}, which is 1.6 times higher than the long-term convergence rate of 50 km Myr^{-1} used to reproduce most data. By assuming that increasing the rate of deformation by 1.6 over 1 Myr does not produce significant modifications of the bulk mechanics of the orogenic wedge, the incoming flux of material and the velocities in the wedge are likely to be increased by the same factor. Hence, we have multiplied the predicted shortening rates by a factor 1.6. The good agreement between results, presented in the following, and the observed rates validate this hypothesis.

For instance, prediction of shortening rates of 24 and 18 km Myr^{-1} over 1 Myr and 200 kyr across the whole orogen (i.e. between magenta square and yellow dot) give modified values of 38 and 30 km Myr^{-}1, respectively, for the periods considered. These values are comparable with the GPS-derived data indicating shortening rates between 27 and 45 mm yr^{-1} (Yu *et al.* 1997). Over the past 1 Myr, short-term distribution of shortening rates first highlights that deformation preferentially focuses on the most frontal thrusts at rates of 4–5 km Myr^{-1}. This trend is amplified over the past 200 kyr and the rate is 6 km Myr^{-1} (Fig. 11). This corresponds to rates of 6–10 km Myr^{-1} consistent with the lower bound of observed geodetic rates of 4.6 to 27 mm yr^{-1} across the frontal Chukou Fault or other estimates of 12 mm yr^{-1} across the HR (Yu *et al.* 1997) (Fig. 4). The abundant seismically released strain and the occurrence of the Chichi earthquake at the western front further supports this prediction. A consequence of increasing rates in the western front is the widening of the low deformation domain of the hinterland. The predicted rate of lower than 1 km Myr^{-1} is, however, in agreement with GPS studies (Fig. 4). As deformation increases to the West, shortening rates also diminish to 8.2 and even 6.7 km Myr^{-1} across the LVF in the same period. If we consider 4 km accommodated within the PSP, this gives 12.2 km Myr^{-1} in the past 1 Myr. Again by scaling this value with the current convergence rates the modified rates become 19.5 km Myr^{-1}. This value is close to the geodetic surveys for baseline between Lutao Island (Northern Luzon Arc) and the CoR (Fig. 4) as well as present-day estimates across the LVF (Yu *et al.* 1997). In summary, our model better fits the long-term and short-term deformation patterns only if we consider a recent increase of the plate convergence from 50 to 80 km Myr^{-1} in the past 1 Myr.

5.2 Long-term exhumation and metamorphic conditions

An age-distance plot of both predicted and observed AFT, ZFT and ZHe ages is shown in (Fig. 3b) to allow for comparison along the northern and southern transects. Predicted ages are generally in good agreement with observed thermochronometric constraints. Indeed, independent of the studied low thermochronometer the Western foreland is generally devoid of reset thermochronometers. And the eastern Central Range, where the highest metamorphic grades are exposed shows consistent reset ages compatible with the Penglai orogeny (Fig. 3b). A departure from this general decrease of ages toward the east is depicted, along the northern transect, where reset ages in the HR are not reproduced by our model. As a result, our model seems in better agreement with the exhumation pattern across the southern transect.

To allow for a more detailed comparison between predicted thermochronometer ages with thermochronometric constraints we plot the temperature against time recorded by each studied particle (Fig. 12a). The closure temperatures for ZFT, AFT and (U–Th)/He on zircons are assumed to be 220–235, 110 and 180 °C, respectively, in agreement with former studies (Liu *et al.* 2000; Beyssac *et al.* 2007). Fig. 12 shows that black and yellow particles, now exposed in the external part of the collision belt, were never buried below the closure temperature for fission-track annealing of apatite and zircon. As a result, the AFT and ZFT ages for these rocks are expected to be older or close to the depositional ages (unreset or detrital ages) in good consistency AFT and ZFT ages reported in

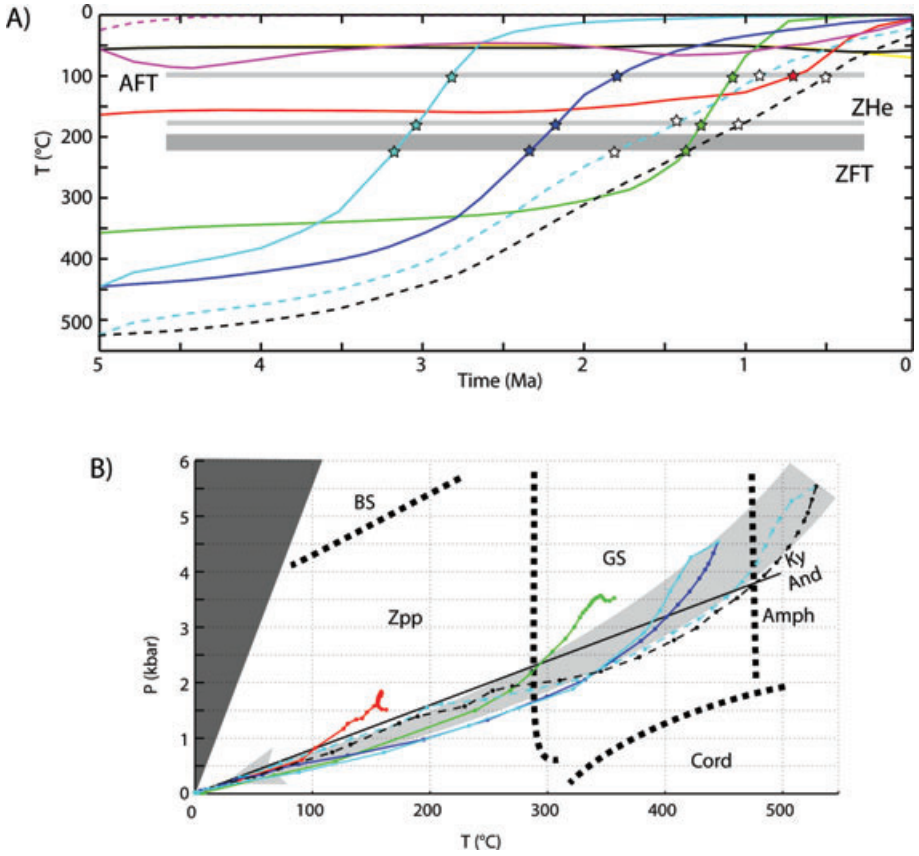

Figure 12. (a) Predicted *T*–*t* paths for particles shown in Fig. 10. Dashed lines correspond to light blue and black squares shown in Fig. 10. Stars show the expected cooling ages of particles with respect to a given thermochronometer. Particle position (not shown here) is recorded every 0.5 Myr. Abbreviations: AFT, closure temperature for Apatite fission tracks; ZFT, closure temperature for Zircon fission tracks; ZHe, closure temperature for (U–Th/He) ages on zircon. (b) *P*–*T* paths for particles studied in in (a). Colours as well as dashed or solid lines refer to captions in (a) (see text for explanation). Dots denote particles position recorded every 0.5 Myr. Such a retrograde evolution follows a classical barrovian HT–LP collisional gradient. Abbreviation: Amph, amphibolite facies; BS, blueschist facies; GS, green schist facies; Zpp, zeolithe-prehnyte-pumpellyite facies; Ky, Kyanite; And, Andalusite and Cord, Cordierite.

Western Taiwan (Fuller *et al.* 2006). The temperature–time trajectory of the red particle indicates unreset ZFT ages but a fully reset AFT age of ∼0.7 Ma. Eastward, the green particle denotes ZFT and AFT ages of 1.4 and 1.2 Ma, respectively consistent with zircon (U–Th/He) age of 1.3 Ma. Eastward, all AFT and ZFT ages appear younger than the Pliocene and thus agree with a cooling event coeval with the Penglai orogeny. Rocks exposed in this domain were all originated at depths greater than 13–14 km but their exhumation show different patterns. The youngest predicted AFT ages lower or close to 1 Ma and ZFT or ZHe ages of 1–2 Ma are associated with the exhumation of the light blue and black squares originated in the deep crust below 16 km. This domain fits well with the AFT ages in the TS that are generally younger than 1 Ma. Assuming a geothermal gradient dT/dz of 30–20 °C km^{-1}, these ages give exhumation rates of 3.6–5.5 mm yr^{-1} consistent with former studies (Willett *et al.* 2003; Lee *et al.* 2006). Eastward, ZFT and AFT ages for light blue and dark blue particles are older ∼3.2–2.4 and 1.8–2.85 Ma, respectively. This reveals that rocks originated at shallower crustal levels and to the west may have been exhumed earlier and thrusted onto rocks of higher metamorphic grades. These predicted ages seem to be in apparent contradiction with the general decrease of reset ages eastward (Fig. 3b). However, this prediction is in good agreement with FT ages of rocks currently exposed in the most immature portion of the southern Central Range (Willett *et al.* 2003; Lee *et al.* 2006). The absence of such rocks in the northern part of the Central Range is likely to be related to the subsequent stages of collision. Indeed, as plate convergence goes on particles with unreset FT ages are eroded and thus removed from the FT ages data set. We infer that rocks originally located east of the assumed TS domain will not record sufficient burial (or subduction) in the past 2 Ma. As a consequence, FT ages predicted in this particular domain are expected to be unreset or partially reset cooling ages in the continental margin. We cannot, however, rule out that some old FT ages may be consistent with an early cooling event during an initial stage of oceanic accretion (Lee *et al.* 2006) but no specific markers in the accretion wedge were studied in this study. We finally infer, based on predicted and observed particle paths, that exhumation of the Central Range agrees with the growth of a large-scale fold as outlined by reset ages along the fold axis and unreset ages on its flanks.

Throughout the modelling pressure–temperature conditions were also computed for all rocks studied in the above section (Fig. 12b). As collision began, the upper crustal rocks entering the orogenic wedge at depths deeper than 10 km, that is, in the greenschist facies or amphibolite facies, are exhumed in the stability field of upper and lower greenschist facies (Fig. 12b). This greenschist metamorphism is observed within the pre-Tertiary basement of the TS and the slates of the BR (Liou 1981). At the end of the modelling, the base of the undisturbed continental crust (lower crust) is in the amphibolite metamorphic facies even sometimes close to the granulite

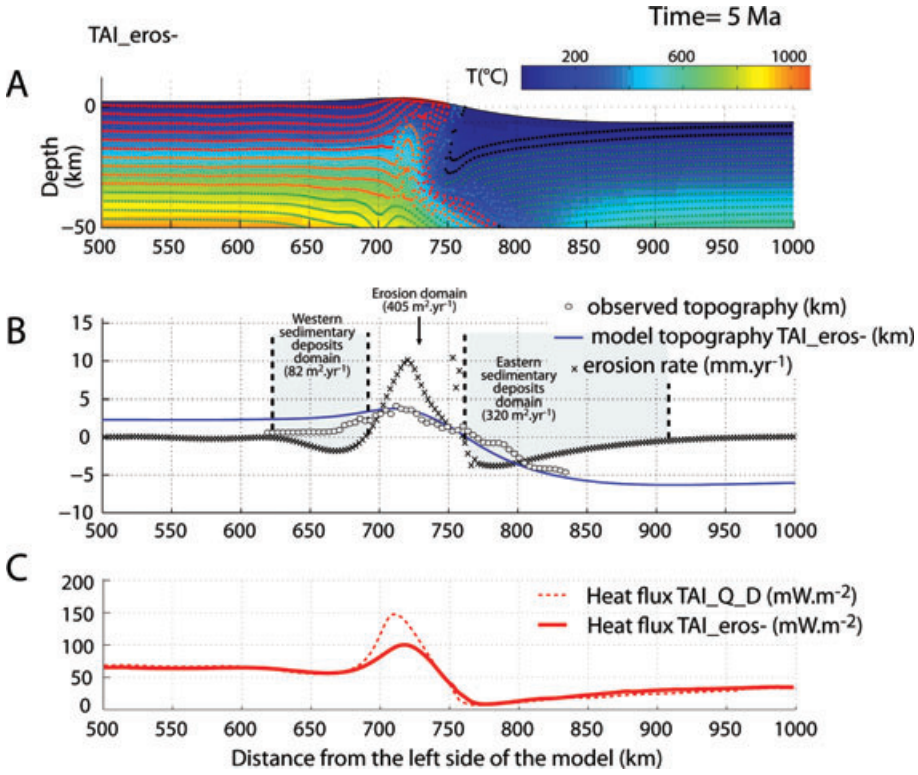

Figure 13. Model results obtained for an erosion coefficient of 2500 m^2 yr^{-1} instead of 5000 m^2 yr^{-1}. (a) Crustal and thermal structure as well as isotherms observed after ∼5 Myr of numerical experiment. (b) Topography and erosion rates associated. (c) Comparison with calculated heat flux of Fig. 5. Lower erosion rates clearly reduce the advection of hot lower crustal material.

metamorphic facies (Fig. 8). At shallower depths, the stable upper crust is under greenschist facies or in the upper grades of the greenschist facies. Peak temperatures recorded by the particles (Fig. 12b) are ranging between 350 (green particle) and 550 °C (dark blue and black particles).

6 SENSITIVITY TO MODEL PARAMETERS

6.1 Erosion rates

Erosion rates are well known to exert a strong control on the exhumation of rocks and hence on mountain building (e.g. Willett 1999). Fig. 13 shows the geotherm and erosion/sedimentation distribution for a model in which the coefficient of erosion is reduced to 2500 m^2 yr^{-1}. The total erosion rates are 402 m^2 yr^{-1} divided into a flux of detrital sediments in the western foreland basin of 82 and 320 m^2 yr^{-1} in the retro-foreland basin. As expected, the erosion rates (Fig. 13b) and consequently the outcoming flux of Eurasian material is lowered (Fig. 13a). The deep crustal isotherms are also less deflected hence reducing the total heat flux at the surface.

The reduction of erosion further leads to the decrease of the predicted cooling rates (Fig. 14a). Moreover only a fraction of the studied particles are exhumed at the end of the numerical experiment. The initiation of cooling is also delayed in time. For instance, the ZFT ages for the light blue and blue dots are estimated to be 2.5 and 0.7 Myr, that is, 1 to 2 Myr younger than observations. Also originally shallower particles (e.g. green and red) are still not exhumed after 5 Myr. Originally deeper particles such as blue squares are also not exhumed at the end of the modelling. This result can be explained by the fact that upward advection of viscous and hot material from the lower crust is inhibited by low erosion. We infer that a coefficient of erosion as high as 5000 m^2 yr^{-1} is required to maintain the long-term exhumation in Taiwan.

6.2 Plate convergence

Hereafter, we test the impact of modifying the plate convergence rates on the exhumation within the collision belt. We first examine the effect of reducing the plate convergence to 25 mm yr^{-1}. Fig. 14b shows that such a reduction obviously results in preventing the exhumation of the upper crust with respect to our preferred model. As a result none of the particles studied in the above sections are exhumed to the surface. For instance, blue particles, which are assumed to represent the most internal portions of the collision belt, are still not exhumed. Moreover, the width of the uplifted domain, which is defined by the intersection between the topographic surface and the crustal rocks, is larger than in our preferred model (Fig. 14b). Interestingly, these patterns of exhumation demonstrate that the reduction of the convergence rates by a factor of two is not equivalent to decrease the duration of the numerical experiment in our reference model. Indeed, a slower plate convergence prevents the decoupling between the upper and the lower crust and the overall strain localization in the model. As a consequence, more distributed shortening results in buckling of a larger portion of the Chinese margin. By contrast, a model for which the convergence rates are close to current geodetic values of 80 mm yr^{-1}, not shown here for the sake of clarity, promotes exhumation during the whole modelling. It finally results in the nearly complete removal of particles by erosion in the reference numerical experiment. We conclude that accelerating or lowering the plate convergence strongly affects the way and the rates to which crustal material are exhumed. This is because

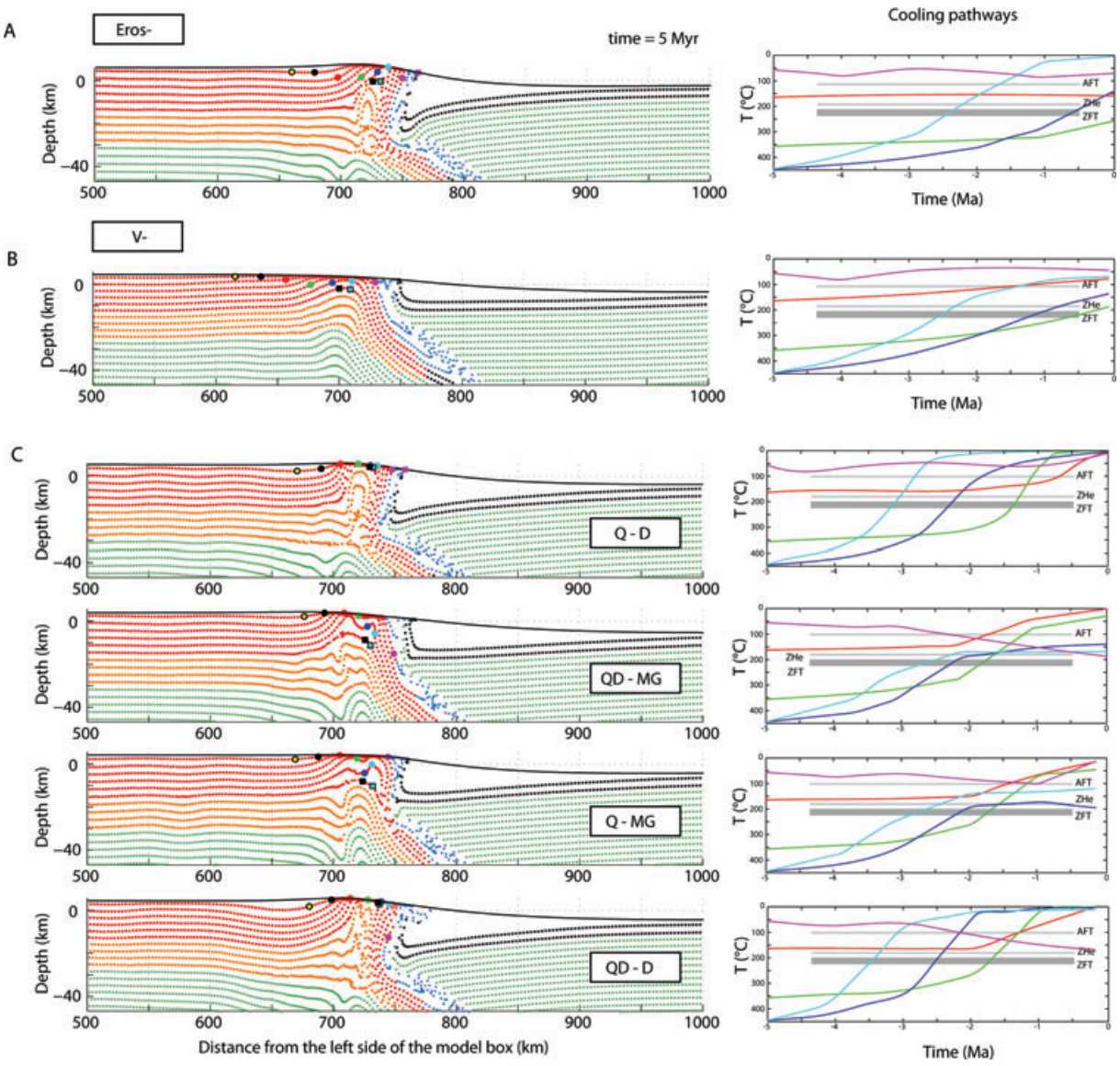

Figure 14. Crustal geometry and cooling history obtained for numerical experiments with reduced erosion, reduced plate convergence or for different combination of crustal composition. Abbreviations: Q, quartz; QD, quartz-diorite; D, diabase and G, mafic granulite. To first order, any modifications that consider (a) lower erosion rates, (b) lower plate convergence or (c) a stronger lower crust (mafic granulite) inhibit the exhumation of the Central Range. This suggests that a weak lower crust (Diabase), fast erosion (5000 m^2 yr^{-1}) and rapid plate convergence (at least 50 km Myr^{-1}) are more suitable for fitting the observed cooling rates.

the plate convergence controls the lithosphere rheology, leading to changes in localization/propagation during mountain building.

6.3 Initial rheology of the continental crust

In our reference numerical experiment, we have assumed a bi-layered continental crust, which was simulated by quartz and diabase rheologies. Alternatively, Mouthereau & Petit (2003) proposed a quartz-diorite and mafic granulite composition to model viscous properties for the upper and lower crust, respectively. Indeed, they showed that a quartz composition for the upper crust is unable to sustain enough stresses to explain the seismicity observed beneath the western foreland down to 12 km. Moreover, a mafic composition for the continental lower crust is acceptable regarding the petrology of the Chinese margin, which was affected by a period of Miocene post-rift magmatism.

Fig. 14c presents a set of models for different rheological profiles in the Eurasian crust together with the corresponding cooling history of particles. Basically, the addition of a stronger lower crust, like in models TAI_QD_MG or TAI_Q_MG (Fig. 14c), inhibits the exhumation process but, however, does not promote the subduction of the upper crust. To first order this seems to be independent of the choice of a relatively weaker (quartz) or stronger upper crust (quartz-diorite) as the exhumation history remains close to that observed in the reference model.

For numerical experiments TAI_ QD_MG and TAI_QD_D where the upper crust is stronger but keeping the lower crust weak we observe that subduction of the magenta dot beneath the PSP is promoted about 3 Ma, which is not observed in other models. In addition, the red particle is exhumed sooner in TAI_QD_D than in the reference experiment. We conclude that any models involving either a stronger upper crust or a stronger lower crust show important

deviation with regard to observations. To first order it is the rheology of the lower continental crust that is predominant in determining the timing of exhumation and hence the mechanism of mountain building. This result is consistent with more complete parametric studies recently conducted with application to Taiwan (Kaus *et al.* 2008).

7 ACCRETION/COLLISION VERSUS SUBDUCTION OF THE CHINESE CONTINENTAL CRUST

Exhumation and *P–T* conditions of rocks as well as the patterns of deformation predicted by our thermodynamic modelling show that crustal rocks of the Chinese margin do not experience significant burial and heating in the subduction zone prior to exhumation. As a result, subduction of the Chinese continental crust appears limited. Although this result may appear controversial it is supported by several evidences that are summarized in the following.

By means of thermochronometric constraints, partially reset or unreset FT data in the southern part of the Central Range, both in the West and in the East of the BS units suggest that part of the continental rocks currently exposed in the Central Range were not buried and reset during the Pliocene (Fig. 3). Moreover, too little evidence for prograde greenschist metamorphism is identified (e.g. in the Chipan gneiss) to definitely support continental subduction. The pervasive penetrative foliations that characterize the higher grade rocks appear consequently to be post-peak. Also, as inferred by previous models, the metamorphic data and model *P–T* paths in the BS suggest a simple cooling and decompression from initial *P–T* conditions in the Chinese passive margin (Simoes *et al.* 2007). In addition, HP-metamorphic rocks in the stable eastern Central Range are restricted to kilometric-scale blocks of metabasites in the Yuli Belt (Fig. 2) whose peak metamorphism is pre-collisional, that is, older than 5 Ma (Beyssac *et al.* 2008). As a consequence, there is currently no evidence for significant syn-subduction metamorphism of the Chinese margin crust.

On the other hand, evidence for fan-shaped slaty S1 cleavages within the TS (Crespi *et al.* 1996) as well as evidence that the marbles of the TS were folded rather than thrusted (Yui & Chu 2000) support the occurrence of a crust-scale fold that is explicitly reproduced in our model. Moreover, viscous deformation beneath the Central Range is currently supported by the low V_P/V_S ratio below 10 km and the relative lack of earthquakes in this area (Rau & Wu 1995; Wu *et al.* 1997; Wu *et al.* 2007). Together with geodetic deformation patterns indicating a lack of shortening beneath the Central Range, these kinematic constraints suggest the existence of an active viscous deformation in association with this large-scale folding. This observation is clearly reproduced in our model as it predicts that viscous thickening would prevail in the lower crust.

Though, some of these data can be accounted for by domains, along a steeply 17°-east-dipping detachment, where underplating vary in time and importance (Simoes *et al.* 2007), we suggest that much of the observations across Taiwan can be more straightforwardly interpreted by the present model. If correct, deformation and exhumation in Taiwan can be accounted for by nearly 100 per cent of frontal accretion of the Asian crust above a gently-dipping décollement located at a depth of ∼25 km.

8 CONCLUSIONS

In this study, we have presented a fully coupled thermomechanical numerical model that satisfactorily reproduces available thermochronometric data, long-/short-term deformation patterns as well as geological observations regarding the past 5 Myr evolution of the Taiwan mountain building. Our thermomechanical model supports earlier hypotheses, thick-skinned in type for which at least the upper 25 km of the Chinese margin crust are accreted in the collision process (Wu *et al.* 1997; Lin *et al.* 1998; Lin 2000). Also in agreement with the previous kinematic models (e.g. Simoes *et al.* 2007), we found that deep seated flux of material from the Chinese crust toward the orogenic wedge should be invoked to compensate for exhumation and erosion in the Central Range. However, instead of being related to underplating that focuses in domains that vary in time and length, it is the consequence of the frontal accretion of the whole bi-layered Asian continental crust. Modelling of *P–T* conditions illustrates that rocks of the Central Range mostly inherited their peak temperatures and pressures in the stable Chinese margin. This finding implies that the eastward increase of metamorphic grades observed across the orogen is likely to be related to the deeper initial position of rocks within the upper crust not to significant subduction prior to exhumation. In any case, the subduction of the Chinese continental crust appears limited. We finally infer that the model presented in this study is in good agreement with the basic expectation that the hot/young and buoyant Chinese continental margin should hardly be subducted beneath the cold/old and dense oceanic plate of the Philippines Sea.

ACKNOWLEDGMENTS

This work has been financially supported by the INSU/Relief program. The authors wish to thank Joerg Denner, T. Gerya and an anonymous reviewer for their insightful comments. Heat flow data were kindly provided by Prof. Kuo-Fong Ma. FM is particularly grateful to K.-F. Ma and A.T. Lin, from the Geophysics Department of NCU (Chungli, Taiwan). We also thank S. Castelltort and B. Kaus from ETH-Zurich for stimulating discussions.

REFERENCES

Barr, T.D. & Dahlen, F.A., 1989. Brittle frictional mountain builiding, 2: thermal structure and heat budget, *J. geophys. Res.,* **94**(B4), 3923–3947.

Beaumont, C., Jamieson, R.A., Nguyen, M.H. & Lee, B., 2001. Himalayan tectonics explained by extrusion of a low-viscosity crustal channel coupled to focused surface denudation, *Nature,* **414**(6865), 738–742.

Beyssac, O., Simoes, M., Avouac, J.P., Farley, K.A., Chen, Y.-G., Chan, Y.-C. & Goffé, B., 2007. Late Cenozoic metamorphic evolution and exhumation of Taiwan, *Tectonics,* **26**(TC6001), doi:10.1029/2006TC002064.

Beyssac, O., Negro, F., Simoes, M., Chan, Y.C. & Chen, Y.G., 2008. High-pressure metamorphism in Taiwan: from oceanic subduction to arc-continent collision? *Terra Nova,* **20,** 118–125.

Bonilla, M.G., 1977. Summary of quaternary faulting and elevation changes in Taiwan, *Geol. Soc. China Mem.,* **2,** 43–55.

Burg, J.-P. & Gerya, T.V., 2005. Viscous heating and thermal doming in orogenic metamorphism: numerical modeling and geological implications, *J. Metamorph. Geol.,* **23,** 75–95.

Burov, E.B. & Diament, M., 1995. Effective elastic thickness of the continental lithosphere—what does it really mean? *J. geophys. Res.,* **100,** 3905–3927.

Burov, E. & Toussaint, G., 2007. Surface processes and tectonics: forcing of continental subduction and deep processes, *Global Planet. Change (Topography of Europe)*, doi:10.1016/j.gloplacha.2007.02.009.

Burov, E. & Yamato, P., 2007. Continental plate collision, P-T-t-z conditions and unstable vs. stable plate dynamics: insights from thermo-mechanical modelling, *Lithos,* **103,** 178–204.

Burov, E., Jolivet, L., Le Pourhiet, L. & Poliakov, A., 2001. A thermomechanical model of exhumation of high pressure (HP) and ultra-high pressure

(UHP) metamorphic rocks in Alpine-type collision belts, *Tectonophysics,* **342**(1–2), 113–136.

Byerlee, J., 1978. Friction of rocks, *Pure appl. Geophys.,* **116,** 615–626.

Carter, N.L. & Tsenn, M.C., 1987. Flow properties of continental lithosphere, *Tectonophysics,* **136,** 27–63.

Chemenda, A.I., Yang, R.-K., Stephan, J.-F., Konstantinovskaya, E.A. & Ivanov, G.M., 2001. New results from physical modelling of arc-continent collision in Taiwan: evolutionary model, *Tectonophysics,* **333,** 159–178.

Chen, C.-H., Chu, H.-T., Liou, J.-G. & Ernst, W.-G., 1983. Explanatory notes for the metamorphic facies map of Taiwan, *Spec. Pub. Central Geol. Surv.,* **2,** 1–3.

Clarck, M.B., Fisher, D.M., Lu, C.-Y. & Chen, C.-H., 1993. Kinematic analyses of the Hsuehshan Range, Taiwan: a large-scale pop-up structure, *Tectonics,* **12,** 205–217.

Clift, P., Lin, J. & Barckhausen, U., 2002. Evidence of low flexural rigidity and low viscosity lower continental crust during continental break-up in the South China Sea, *Mar. Petrol. Geol.,* **19,** 951–970.

Crespi, J., Chan, Y.C. & Swaim, M.S., 1996. Synorogenic extension and exhumation of the Taiwan hinterland, *Geology,* **24**(3), 247–250.

Cruciani, C., Carminati, E. & Doglioni, C., 2005. Slab dip vs. lithosphere age: no direct function, *Earth planet. Sci. Lett.,* **238**(3–4), 298–310.

Cundall, P.A., 1989. Numerical experiments on localization in frictional materials, *Ing. Arch.,* **59,** 148–159.

Currie, C.A., Beaumont, C. & Huismans, R.S., 2007. The fate of subducted sediments: a case for backarc intrusion and underplating, *Geology,* **35,** 1111–1114.

Dadson, S.J. *et al*., 2003. Links between erosion, runoff variability and seismicity in the Taiwan orogen, *Nature,* **426,** 648–651.

Dahlen, F.A. & Barr, T.D., 1989. Brittle frictional mountain building, 1: deformation and mechanical energy budget, *J. geophys. Res.,* **94,** 3906–3922.

Dahlen, F.A., Suppe, J. & Davis, D., 1984. Mechanics of fold-and-thrust belts and accretionary wedges: cohesive coulomb theory, *J. geophys. Res.,* **89**(B12), 10 087–10 101.

Davis, D., Suppe, J. & Dahlen, F.A., 1983. Mechanics of fold-and-thrust belts and accretionary wedges, *J. geophys. Res.,* **88**(B2), 1153–1172.

De Capitani, C., 1994. Gleichgewichts-Phasendiagramme : Theorie und Software, Jahrestagung der Dtsch. Mineral. Ges., *Beihefte zum European J. Mineral,* **6,** 1–48.

Deschamps, A., Monie, P., Lallemand, S., Hsu, S.-K. & Yeh, K.Y., 2000. Evidence for Early Cretaceous oceanic crust trapped in the Philippine Sea Plate, *Earth planet. Sci. Lett.,* **179**(3–4), 503–516.

Ernst, W.G., 1981. Petrotectonic settings of glaucophane schist belts and some implications for Taiwan, *Geol. Soc. China Mem.,* **4,** 229–267.

Faccenda, M., Gerya, T.V. & Chakraborty, S., 2008. Styles of post-subduction collisional orogeny: influence of convergence velocity, crustal rheology and radiogenic heat production, *Lithos,* **103,** 257–287.

Fisher, D.M., Lu, C.-Y. & Chu, H.T., 2002. Taiwan Slate Belt: Insights into the ductile interior of an arc-continent collision, in *Geology and Geophysics of an Arc-Continent collision, Taiwan, Republic of China, Geological Society of America Special Paper,* Vol. 358, pp. 93–106, eds Byrne, T.B. & Liu, C.-S., GSA, Boulder, CO.

Fuller, C., Willett, S.D., Fischer, D. & Lu, C.-Y., 2006. A thermomechanical wedge model of Taiwan constrained by fission-track thermochronometry, *Tectonophysics,* **425,** 1–24.

Gerya, T.V., Perchuk, L.L. & Burg, J.-P., 2008. Transient hot channels: perpetrating and regurgitating ultrahigh-pressure, high temperature crust-mantle associations in collision belts, *Lithos,* **103,** 236–256.

Goetze, C., 1978. The mechanics of creep in Olivine, *Phil. Trans. R. Soc. Lond.,* **288,** 99–119.

Hansen, F.D. & Carter, N.L., 1982. Creep of selected crustal rocks at 1000 MPa, *EOS, Trans. Am. geophys Un.,* **63,** 437.

Ho, C.-S., 1986. A synthesis of the geologic evolution of Taiwan, *Tectonophysics,* **125,** 1–16.

Huang, C.-Y., Yuan, P.B., Song, S.-R., Lin, C.-W., Wang, C., Chen, M.-T., Shyu, C.-T. & Karp, B., 1995. Tectonics of short-lived intra-arc basins in the arc-continent collision terrane of the Coastal Range, eastern Taiwan, *Tectonics,* **14**(1), 19–38.

Kaus, B., Steeman, C. & Becker, T.W., 2008. From passive continental margin to mountain belt: insights from analytical and numerical models and application to Taiwan, *Phys. Earth planet. Int.,* doi:10.1016/j.pepl.2008.06.015.

Le Pourhiet, L., Burov, E. & Moretti, I., 2004. Rifting through a stack of inhomogeneous thrusts (the dipping pie concept), *Tectonics,* **23**(TC4005), doi:10.1029/2003TC001584.

Lee, C.-R. & Cheng, W.-T., 1986. Preliminary heat flow measurements in Taiwan, in *Proceedings of the Fourth Circum-Pacific Energy and Mineral Resources Conference,* 1986, Singapor.

Lee, T.-Y. & Lawver, L.A., 1995. Cenozoic plate reconstruction of Southeast Asia, *Tectonophysics,* **251,** 85–138.

Lee, J.-C., Angelier, J. & Chu, H.-T., 1997. Polyphase history and kinematics of a complex major fault zone in the northern Taiwan mountain belt : the Lishan fault, *Tectonophysics,* **274,** 97–115.

Lee, Y.-H., Chen, C.-C., Liu, T.-K., Ho, H.-C., Lu, H.-Y. & Lo, W, 2006. Mountain building mechanisms in the southern Central Range of the Taiwan orogenic belt from accretionary wedge deformation to arc-continent collision, *Earth planet. Sci. Lett.,* **252**, 413–422.

Li, Y.-H., 1976. Denudation of Taiwan Island since the Pliocene epoch, *Geology,* **4,** 105–107.

Lin, C.-H., 2000. Thermal modeling of continental subduction and exhumation constrained by heat flow and seismicity in Taiwan, *Tectonophysics,* **324,** 189–201.

Lin, C.-H., Yeh, Y.-H., Yen, H.-Y., Chen, K.-C., Huang, B.-S., Roecker, S.W. & Chiu, J.-M., 1998. Three-dimensional elastic wave velocity structure of the Hualien region of Taiwan: evidence of active crustal exhumation, *Tectonics,* **17**(1), 89–103.

Lin, A.T., Watts, A.B. & Hesselbo, S.P., 2003. Cenozoic stratigraphy and subsidence history of the South China Sea margin in the Taiwan region, *Basin Res.,* **15**(4), 453–478.

Liou, J.-G., 1981. Petrology of metamorphosed oceanic rocks in the Central Range of Taiwan, *Geol. Soc. China Mem.,* **4,** 291–341.

Liou, J.G. & Ernst, W.G., 1984. Summary of phanerozoic metamorphism in Taiwan, *Geol. Soc. China Mem.,* **6**(December 1984), 133–152.

Liu, T.-K., Chen, Y.-G., Chen, W.-P. & Jiang, S.-H., 2000. Rates of cooling and denudation of the early Penglai orogeny, Taiwan, as assessed by fission-track constraints, *Tectonophysics,* **320,** 69–82.

Lo, C.-H. & Onstott T.C., 1995. Rejuvenation of K-Ar systems for minerals in the Taiwan mountain belt, *Earth planet. Sci. Lett.,* **131,** 71–98.

Lundberg, N. & Dorsey, R.J., 1990. Rapid quaternary emergence, uplift, and denudation of the Coastal Range, eastern Taiwan, *Geology,* **18,** 638–641.

Ma, K.-F. & Song, D.-R., 1997. In velocity and Moho depth in Taiwan, *J. Geol. Soc. China,* **40,** 167–184.

Mouthereau, F. & Lacombe, O., 2006. Inversion of the Paleogene Chinese continental margin and thick-skinned deformation in the Western Foreland of Taiwan, *J. Struct. Geol.,* **28,** 1977–1993.

Mouthereau, F. & Petit, C., 2003. Rheology and strength of the Eurasian continental lithosphere in the foreland of the Taiwan collision belt : constraints from seismicity, flexure and structural styles, *J. geophys. Res.,* **108**(B11), 2512, doi:10.1029/2002JB002098.

Mouthereau, F., Lacombe, O., Deffontaines, B., Angelier, J. & Brusset, S., 2001. Deformation history of the southwestern Taiwan foreland thrust belt: insights from tectono-sedimentary analyses and balanced cross-sections, *Tectonophysics,* **333,** 293–322.

Parsons, B. & Sclater, J.G., 1977. An analysis of the variation of ocean floor bathymetry and heat flow with age, *J. geophys. Res.,* **82,** 803–827.

Peng, T.-H., Li, Y.H. & Wu, F.T., 1977. Tectonic uplift rates of the Taiwan island since the early Holocene, *Mem. Geol. Soc. China,* **2,** 57–69.

Poliakov, A., Podladchikov, Y. & Talbot, C.J., 1993. Initiation of salt diapirs with frictional overburden : numerical experiments, *Tectonophysics,* **228,** 199–210.

Pulver, M.H., Crespi, J.M. & Byrne, T.B., 2002. Lateral extrusion in a transpressional collision zone: an example from the pre-Tertiary metamorphic basement of Taiwan, in *Geology and Geophysics of an Arc-Continent collision, Taiwan, Republic of China, Geological Society of America Special Paper,* Vol. 358, pp. 107–120, eds Byrne, T.B. & Liu, C.-S. GSA, Boulder, CO.

Ranalli, G. & Murphy, D.C., 1987. Rheological stratification of the lithosphere, *Tectonophysics,* **132,** 281–295.

Rau, R.-J. & Wu, F.T., 1995. Tomographic imaging of lithospheric structures under Taiwan, *Earth planet. Sci. Lett.,* **133,** 517–532.

Sibuet, J.-C. & Hsu, S.-K., 2004. How was Taiwan created? *Tectonophysics,* **379,** 159–181.

Sibuet, J.-C., Hsu, S.-K., Le Pichon, X., Le Formal, J.P., Reed, D., Moore, G. & Liu, C.-S., 2002. East Asia tectonics since 15 Ma: constraints from the Taiwan region, *Tectonophysics,* **344,** 103–134.

Simoes, M. & Avouac, J.P., 2006. Investigating the kinematics of mountain building in Taiwan from the spatiotemporal evolution of the foreland basin and western foothills, *J. geophys. Res.,* **111**(B10401), doi:10.1029/2005JB004209.

Simoes, M., Avouac, J.-P., Beyssac, O., Goffe, B., Farley, K.A. & Chen, Y.-G., 2007. Mountain building in Taiwan: a thermokinematic model, *J. geophys. Res.,* **112**(B11405), doi:10.1029/2006JB004824.

Sobolev, S.V. & Babeyko, A.Y., 2005. What drives orogeny in the Andes? *Geology,* **33,** 617–620.

Suppe, J., 1981. Mechanics of mountain building and metamorphism in Taiwan, *Geol. Soc. China Mem.,* **4,** 67–89.

Taylor, B. & Hayes, D.E., 1980. The Tectonic Evolution of the South China Basin, in *The Tectonic and Geological Evolution of the Southeast Asian Seas and Islands, Geophysical Monograph Series,* Vol. 23, pp. 89–104, ed. Hayes, D.E., American Geophysical Union, Washington, D.C.

Teng, L.-S., 1990. Geotectonic evolution of late Cenozoic arc-continent in Taiwan, *Tectonophysics,* **183,** 67–76.

Teng, L.-S., 1992. Geotectonic evolution of Tertiary continental margin basins of Taiwan, *Petrol. Geol. Taiwan,* **27,** 1–19.

Tensi, J., Mouthereau, F. & Lacombe, O., 2006. Lithospheric bulge in the West Taiwan Basin, *Basin Res.,* **18**(3), 277–299.

Tillman, K.S. & Byrne, T.B., 1995. Kinematic analysis of the Taiwan slate belt, *Tectonics* **14**(7), 322–341.

Toussaint, G., Burov, E. & Jolivet, L., 2004a. Continental plate collision: unstable versus stable slab dynamics, *Geology,* **32**(1), 33–36.

Toussaint, G., Burov, E. & Avouac, J.-P., 2004b. Tectonic evolution of a continental collision zone: a thermo mechanical numerical model, *Tectonics,* **23,** TC6003, doi:10.1029/2003TC001604.

Turcotte, D.L. & Schubert, G., 2002. *Geodynamics: Applications of Continuum Mechanics to Geological Problems,* Cambridge University Press.

Watts, A.B. & Burov, E., 2003. Lithospheric strength and its relationship to the elastic and seismogenic layer thickness, *Earth planet. Sci. Lett.,* **213,** 113–131.

Warren, C.J., Beaumont, C. & Jamieson, R.A., 2008. Modelling tectonic styles and ultra-high pressure (UHP) rock exhumation during the transition from oceanic subduction to continental collision, *Earth. planet. Sci. Lett.,* **267,** 129–145.

Wilks, K.R. & Carter, N.L., 1990. Rheology of some continental lower crust, *Tectonophysics,* **182,** 57–77.

Willett, S.D., 1999. Orogeny and orography: the effects of erosion on the structure of mountain belts, *J. geophys. Res.,* **164**(B12), 28 957–28 981.

Willett, S.D. & Brandon, M.T., 2002. On steady states in mountain belts, *Geology,* **30,** 175–178.

Willett, S.D., Fischer, D., Fuller, C., Yeh, E.-C. & Lu, C.-Y., 2003. Erosion rates and orogenic-wedge kinematics in Taiwan inferred from fission-track thermochronometry, *Geology,* **31**(11), 945–948.

Wu, F.T., Rau, R.-J. & Salzberg, D., 1997. Taiwan orogeny: thin-skinned or lithospheric collision, *Tectonophysics,* **274,** 191–220.

Wu, Y.-M., Chang, C.-H., Zhao, L., Bruce, J., Shyu, H., Chen, Y.-G., Sieh, K. & Avouac, J.-P., 2007. Seismic tomography of Taiwan: improved constraints from a dense network of strong motion stations, *J. geophys. Res.,* **112**(B08312), doi:10.1029/2007JB004983.

Yamato, P., Agard, P., Burov, E., Le Pourhiet, L., Jolivet, L. & Tiberi, C., 2007. Burial and exhumation in a subduction wedge: Mutual constraints from thermomechanical modeling and natural P-T-t data (Schistes Lustrés, western Alps), *J. geophys. Res.,* **112**(B07410), doi:10.1029/2006JB004441.

Yamato, P., Burov, E., Agard, P., Le Pourhiet, L. & Jolivet, L., 2008. HP-UHP exhumation during slow continental subduction: Self-consistent thermodynamically and thermomechanically coupled model with application to the Western Alps, *Earth. planet. Sci. Lett.,* **271,** 63–74.

Yen, H.-Y., Yeh, Y.-H. & Wu, F.T., 1998. Two-dimensional crustal structures of Taiwan from gravity data, *Tectonics,* **17**(1), 104–111.

Yu, S.-B., Chen, H.-Y. & Kuo, L.-C., 1997. Velocity field of GPS stations in the Taiwan area, *Tectonophysics,* **274,** 41–59.

Yue, L.-F., Suppe, J. & Hung, J.-H., 2005. Structural geology of a classic thrust belt earthquake: the 1999 Chi-Chi earthquake Taiwan (Mw = 7.6), *J. Struct. Geol.,* **27,** 2058–2083.

Yui, T.-F. & Chu, H.-T., 2000. 'Overturned' marble layers: evidence for upward extrusion of the Backbone Range of Taiwan, *Earth planet. Sci. Lett.,* **179,** 351–361.